

A comprehensive picture for binary interactions of subaqueous barchans

Erick Franklin^{1,1,1} and Willian Righi Assis^{1,1,1}

¹UNICAMP - University of Campinas

November 30, 2022

Abstract

We investigate experimentally the short-range interactions occurring between two subaqueous barchans. The experiments were conducted in a water channel of transparent material where controlled grains were poured inside, and a camera placed on the top acquired images of the bedforms. We varied the grain types (diameter, density and roundness), pile masses, transverse distances, water flow rates and initial conditions. As a result, five different patterns were identified for both aligned and off-centered configurations and we propose interaction maps that depend basically on the ratio between the number of grains of each dune, Shields number and alignment of barchans. In addition, we show experimental evidence that an ejected barchan has roughly the same mass of the impacting one in some cases, and that in wake-dominated processes the asymmetry of the downstream dune is large. The present results shed light on the size regulation of barchans found on Earth and other planets.

A comprehensive picture for binary interactions of subaqueous barchans

An edited version of this paper was published by AGU. Copyright 2020 American Geophysical Union.

Assis, W. R. and Franklin, E. M. (2020). A comprehensive picture for binary interactions of subaqueous barchans. *Geophysical Research Letters*, 47, e2020GL089464, DOI 10.1029/2020GL089464.

To view the published open abstract, go to <https://doi.org/10.1029/2020GL089464>.

W. R. Assis¹, E. M. Franklin²

^{1,2}School of Mechanical Engineering, UNICAMP - University of Campinas,
Rua Mendeleev, 200, Campinas, SP, Brazil

Key Points:

- We identify five binary interactions of barchans and propose classification maps
- We show indications that an ejected barchan has the same mass of the impacting one
- We found that the asymmetry of the downstream dune is large in wake-dominated processes

Corresponding author: Erick M. Franklin, franklin@fem.unicamp.br

Abstract

We investigate experimentally the short-range interactions occurring between two subaqueous barchans. The experiments were conducted in a water channel of transparent material where controlled grains were poured inside, and a camera placed on the top acquired images of the bedforms. We varied the grain types (diameter, density and roundness), pile masses, transverse distances, water flow rates and initial conditions. As a result, five different patterns were identified for both aligned and off-centered configurations and we propose interaction maps that depend basically on the ratio between the number of grains of each dune, Shields number and alignment of barchans. In addition, we show experimental indications that an ejected barchan has roughly the same mass of the impacting one in some cases, and that in wake-dominated processes the asymmetry of the downstream dune is large. The present results shed light on the size regulation of barchans found on Earth and other planets.

Plain Language Summary

Barchans are crescent-shaped dunes that are often organized in dune fields, where binary interactions and collisions play a significant role in regulating their dynamics and sizes. Barchan collisions are frequent in many environments, such as Earth's deserts and on the surface of Mars, but their large time scales (the decade and the millennium for aeolian and Martian collisions, respectively) compared to the aquatic case (of the order of the minute) make subaqueous barchans the ideal object of study. Taking advantage of that, we performed experiments in a water channel of transparent material, where pairs of barchans were transported by the water flow while a camera acquired images of them. We found five different types of barchan-barchan interaction, and propose maps that provide a comprehensive classification for the short-range interactions of subaqueous barchans. In addition, we show that, in some cases, an ejected barchan has roughly the same mass of the impacting one, and that the perturbation of the flow caused by the upstream barchan generates large asymmetries in the downstream one. Our results represent a significant step toward understanding the barchanoid forms and size regulation of barchans found in water, air, and other planetary environments.

1 Introduction

The interaction between a fluid flow and a granular bed gives rise to different kinds of bedforms. Of particular interest are the crescent-shaped dunes, called barchans, that are formed under one-directional flow and limited amount of available grains, being encountered in different environments such as rivers, water ducts, Earth's deserts and other planetary environments (Bagnold, 1941; Herrmann & Sauermann, 2000; Hersen, 2004; Elbelrhiti et al., 2005; Claudin & Andreotti, 2006; Parteli & Herrmann, 2007). Although barchans may grow as isolated bedforms (Alvarez & Franklin, 2017, 2018), they are often organized in dune fields, where dune-dune interactions play a significant role in regulating their dynamics and sizes (Hersen et al., 2004; Hersen & Douady, 2005; Kocurek et al., 2010; Génois, Hersen, et al., 2013; Génois, du Pont, et al., 2013).

Over the past decades, several studies investigated the collisions and short-distance interactions of aeolian barchans based on field measurements (Norris & Norris, 1961; Gay, 1999; Vermeesch, 2011; Hugenholtz & Barchyn, 2012). Yet, because these measurements are based on aerial images, the time series for barchan collisions are usually incomplete given the long timescales of aeolian interactions (of the order of the decade), hindering a comprehensive understanding of barchan collisions. Because of their much faster scales (of the order of the minute), some studies investigated the interactions of barchans in water flumes and tanks (Endo et al., 2004; Hersen & Douady, 2005), from which different collision patterns were identified and their dynamics described. In addition, numerical simulations using continuum (Schwämmle & Herrmann, 2003; Durán et al., 2005;

68 Zhou et al., 2019) and simplified discrete models (Katsuki et al., 2011) could reproduce
69 some of the collision patterns, shedding light on the essential mechanisms involved. How-
70 ever, the simplifications present in those models precluded them from reproducing cor-
71 rectly all barchan interactions, failing to predict the correct split of dunes in some cases
72 and predicting soliton behavior in others.

73 By observing that a solitary barchan within a dune field is marginally stable, tend-
74 ing to grow or shrink once the stable size is disturbed, and the existence in nature of cor-
75 ridors of barchans, Hersen et al. (2004) proposed a model for the formation of corridors,
76 and Hersen and Douady (2005) showed that barchan collisions could be important for
77 the size regulation of barchans. In order to better understand the mechanisms behind
78 the formation of corridors with size-selected barchans, Durán et al. (2009) and Génois,
79 du Pont, et al. (2013) introduced simplified models based on sand flux balances and el-
80 elementary rules for barchan collisions. With such models, Durán et al. (2009) showed that
81 collisions are important for size regulation and inter-barchan spacing, while Génois, du
82 Pont, et al. (2013), by adjusting sand fluxes, obtained corridors of sparse and large or
83 dense and small barchans according to the balance between sand fluxes and collision types,
84 showing that sand distribution due to collisions organizes barchans in narrow corridors
85 of size-selected dunes. Bo and Zheng (2013), based on numerical simulations using a scale-
86 coupled model, found that the probability of barchan collisions varies with the flow strength,
87 grain diameter, grain supply and height ratio of barchans. They quantified the proba-
88 bilities for the occurrence of three different types of barchan collisions within a dune field
89 (merging, exchange and fragmentation-exchange, described next), but not how the col-
90 lision processes vary with the considered parameters.

91 Although many previous studies were devoted to barchan collisions, the problem
92 is still not completely understood and a general picture is lacking. The emerging pat-
93 terns, though present in both aeolian and aquatic environments, have not yet had all their
94 important parameters identified, so that universal expressions or maps for predicting the
95 results of collisions do not exist. The identification of collision patterns from the approach-
96 ing of subaqueous barchans until the end of the collisional process was performed by Endo
97 et al. (2004) in the case of aligned dunes for different mass ratios, and by Hersen and
98 Douady (2005) in the case of off-centered dunes for different transverse distances of cen-
99 troids of colliding dunes (referred to as impact or offset parameter), while Bo and Zheng
100 (2013) focused on the probabilities of barchan collisions in a dune field obtained from
101 numerical computations. However, how the diameter, density and roundness of grains,
102 flow strength and initial conditions affect the collision patterns remains to be investigated.
103 In addition, mass transfers between barchans during collisions are not completely un-
104 derstood.

105 In this Letter we investigate extensively the binary interactions, including binary
106 collisions, of subaqueous barchans. We carried out exhaustive measurements of the short-
107 range interactions between two barchan dunes, i.e., when their longitudinal separation
108 is of the order of the size of the upstream bedform, by varying the mass of initial piles,
109 their alignment (centered or off-centered), initial longitudinal separation, grain proper-
110 ties (diameter, density and roundness), flow strength and initial conditions (downstream
111 barchan already formed or to be developed), most of them affecting the patterns emerg-
112 ing from interactions. We identify five types of binary interactions for both aligned and
113 off-centered barchans, and show indications that an ejected barchan has roughly the same
114 mass of the impacting one in cases involving collisions with exchange of grains and that
115 in wake-dominated processes the asymmetry of the downstream dune is large. We pro-
116 pose a new classification for the binary short-range interactions of subaqueous barchans
117 that depends on the ratio between the number of grains of each dune, Shields number
118 and barchans alignment, shedding light on the size regulation of barchans in a dune field.

2 Materials and Methods

The experimental device consisted of a water reservoir, two centrifugal pumps, a flow straightener, a 5-m-long closed-conduit channel of transparent material and rectangular cross section (width = 160 mm and height $2\delta = 50$ mm), a settling tank, and a return line. A pressure-driven flow was imposed in the channel by means of the centrifugal pumps, and the flow followed the order just described. The channel test section was 1 m long and started 40 hydraulic diameters, $40 \times d_h$, downstream of the channel inlet, assuring a developed channel flow just upstream of the bedforms, where $d_h = 3.05 \delta$ is the cross-sectional area multiplied by four and divided by the cross-sectional perimeter. With the channel previously filled with water, controlled grains were poured inside, forming a pair of bedforms in either aligned or off-centered configurations. By imposing a water flow, each bedform was deformed into a barchan shape and interacted with each other. We used different initial conditions, in which we placed a first pile and let it deform into a barchan dune before placing an upstream pile, or we let it deform in half-way a barchan dune before placing the second pile, or we placed two conical piles and let them deform together into barchan dunes, and the mass ratio of the piles, defined here as the mass of the upstream pile (impacting) divided by that of the downstream one (target), varied within 0.005 and 1. The initial longitudinal distance between bedforms was of the order of the diameter of the upstream pile, D , being within 0.22 and $3.6D$ between dune borders (smaller distance between dunes in the longitudinal direction), and, because the dune velocity varies with the inverse of its size (Bagnold, 1941), the mass of the impacting dune was always equal or lesser than that of the target dune. A camera placed above the channel acquired images of the bedforms and, therefore, we did not measure systematically the barchan height. However, based on reported values of the aspect ratio of barchans (Andreotti et al., 2002a) and our experimental observations, we estimate the crest heights as approximately 5 mm, i.e., 10 % of the channel height. The layout of the experimental device, a photograph of the test section, and microscopy images of the used grains are shown in the supporting information.

A total number of 123 tests were performed, for which we used tap water at temperatures within 22 and 30 °C and different populations of grains (not mixed): round glass beads ($\rho_s = 2500$ kg/m³) with $0.15 \text{ mm} \leq d \leq 0.25 \text{ mm}$ and $0.40 \text{ mm} \leq d \leq 0.60 \text{ mm}$, angular glass beads with $0.21 \text{ mm} \leq d \leq 0.30 \text{ mm}$, and zirconium beads ($\rho_s = 4100$ kg/m³) with $0.40 \text{ mm} \leq d \leq 0.60$, where ρ_s and d are, respectively, the density and diameter of grains. The cross-sectional mean velocities of water, U , varied between 0.226 and 0.365 m/s, corresponding to Reynolds numbers based on the channel height, $\text{Re} = \rho U 2\delta / \mu$, within 1.13×10^4 and 1.82×10^4 , where μ is the dynamic viscosity and ρ the density of the fluid. The shear velocities on the channel walls (base state), u_* , were computed based on measurements with a two-dimensional particle image velocimetry (2D-PIV) device (Franklin et al., 2014; Cúñez et al., 2018; Alvarez & Franklin, 2018) and found to follow the Blasius correlation (Schlichting, 2000), being within 0.0133 and 0.0202 m/s. By considering the fluid velocities applied to each grain type, the Shields number, $\theta = (\rho u_*^2) / ((\rho_s - \rho)gd)$, varied within 0.019 and 0.106, where g is the acceleration of gravity (see supporting information for a description of the PIV tests, estimated deviations in u_* and θ , and lists of all tested conditions).

3 Results

Five different patterns were observed as resulting from the short-range interaction, as can be seen in Figures 1 and 2, that show, respectively, snapshots of barchan interactions for the aligned and off-centered cases: 1) chasing (Figures 1a and 2a), when the upstream dune does not reach the downstream one. This pattern appears when the barchans have almost the same size, and the wake of the upstream dune, by increasing turbulent levels and creating channeling (Palmer et al., 2012; Bristow et al., 2018), promotes a larger erosion on the downstream dune, which then shrinks and moves faster (even if it receives

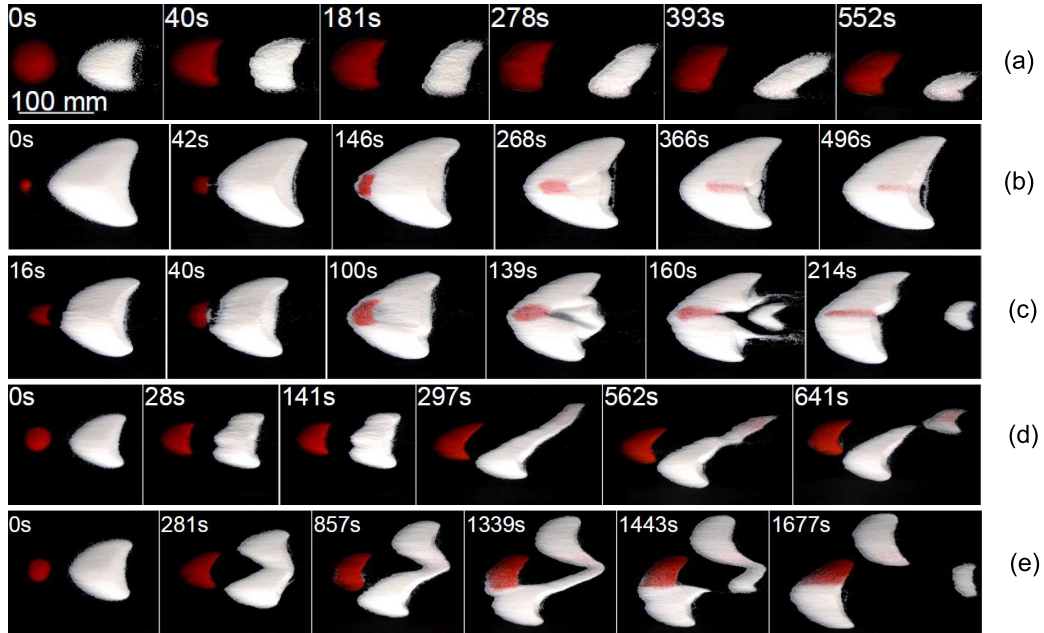


Figure 1. Snapshots of barchan interactions for aligned dunes. In the snapshots, the water flow is from left to right, the upstream pile consisting of red (darker) glass beads and the downstream pile of white (clearer) glass beads, and the corresponding times are shown in each frame. In Figure (a), $0.40 \text{ mm} \leq d \leq 0.60 \text{ mm}$ and in the remaining figures $0.15 \text{ mm} \leq d \leq 0.25 \text{ mm}$. (a) Chasing; (b) merging; (c) exchange; (d) fragmentation-chasing; (e) fragmentation-exchange, and they correspond to test numbers 61, 65, 36, 5 and 22 in the table of Fig. S23 of the supporting information, respectively.

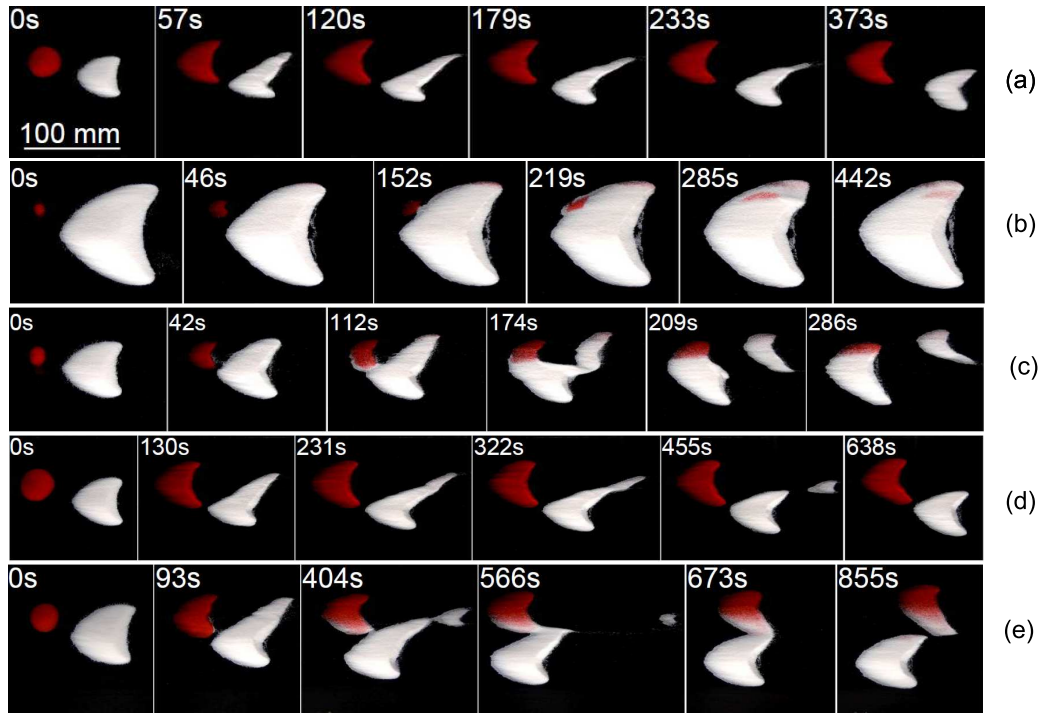


Figure 2. Snapshots of barchan interactions for off-centered dunes. In the snapshots, the water flow is from left to right, the upstream pile consisting of red (darker) glass beads and the downstream pile of white (clearer) glass beads of $0.15 \text{ mm} \leq d \leq 0.25 \text{ mm}$, and the corresponding times are shown in each frame. (a) Chasing; (b) merging; (c) exchange; (d) fragmentation-chasing; (e) fragmentation-exchange, and they correspond to test numbers 43, 38, 41, 31 and 5 in the table of Fig. S24 of the supporting information, respectively.

171 grains from the upstream barchan); 2) merging (Figures 1b and 2b), when the upstream
 172 dune reaches the downstream one and they merge; 3) exchange (Figures 1c and 2c), when,
 173 once the upstream dune reaches the downstream one, a small barchan is ejected and, be-
 174 ing the smaller one, outruns the other and migrates downstream. The first impression
 175 is that the impacting barchan traverses the target one, but the use of marked grains shows
 176 that there is mass exchange between them, as can be seen in Figures 1c and 2c. In some
 177 cases, depending on the sum of sizes of the impacting and target barchans, the ejected
 178 barchan is so small that it is close to the minimum size (Franklin & Charru, 2011) and
 179 spreads out just after being ejected; 4) fragmentation-chasing (Figures 1d and 2d), when,
 180 due to the wake of the upstream dune (Palmer et al., 2012; Bristow et al., 2018), in par-
 181 ticular just downstream the reattachment point of the recirculation region, the down-
 182 stream dune splits before being reached. Because the divided dunes are smaller than the
 183 upstream one, they outrun the upstream dune; and 5) fragmentation-exchange (Figures
 184 1e and 2e), when fragmentation as in (4) initiates, but, the upstream barchan being still
 185 faster than the splitting dune, the former reaches the latter. Once they touch, an off-center
 186 exchange occurs, and a small barchan is ejected. In the aligned configuration, the ejected
 187 barchan results from the interaction of an elongated horn with the remaining of the di-
 188 vided dunes, while in the off-centered configuration the ejected barchan is the smaller
 189 portion of the splitting dune. Finally, this redistribution of grains having finished, the
 190 smaller dunes are downstream and, therefore, three resulting barchans migrate without
 191 reaching each other. Movies showing all the five dune-dune interactions for both con-
 192 figurations and snapshots for other grain types are available as supporting information.

193 The presence of the five patterns in both aligned and off-centered configurations
 194 shows that variations of the offset (or impact) parameter, although influencing the con-
 195 ditions where patterns can appear, are not crucial for their appearance. Also, the mass
 196 ratio alone cannot regulate the appearance of all collision patterns, Endo et al. (2004)
 197 and Durán et al. (2005) having not found the five patterns for aligned dunes by vary-
 198 ing only their mass ratio. Endo et al. (2004) identified only the merging, exchange and
 199 fragmentation-chasing patterns (which they named absorption, ejection and split), and
 200 Durán et al. (2005), based on numerical simulations, the merging and exchange patterns
 201 (which they called coalescence and breeding), but the latter with a different behavior than
 202 our experimental observations. In addition, they found a pattern called budding, which
 203 could be equivalent to the fragmentation-exchange, but, in fact, is different, the target
 204 dune splitting only after the collision had happened, and also a solitary wave behavior,
 205 which is not observed experimentally. However, until now the different patterns emerg-
 206 ing from collisions have been described in terms of only the offset parameter and mass
 207 ratio (Katsuki et al., 2005; Génois, du Pont, et al., 2013; Génois, Hersen, et al., 2013).

208 We observed in our experiments that, in addition to these parameters, the fluid shear-
 209 ing and mass of each grain are also of importance, the latter, combined with the pile masses,
 210 being equivalent to the number of grains forming the piles. If, in one hand, the differ-
 211 ence in the number of grains (or, also, the mass ratio) gives the time scale for collision,
 212 on the other hand the total number of grains (or the sum of pile volumes) gives the to-
 213 tal size of the system, indicating if the resulting barchan is too large, with tendency to
 214 split because of instabilities of hydrodynamic nature (Andreotti et al., 2002a, 2002b; Charru,
 215 2006; Franklin, 2015). In addition, the flow strength and the size and density of grains
 216 are also related to hydrodynamic instabilities and to minimum sizes regulating the wave-
 217 length of bedforms and favoring the split of dunes or even their spread out (Andreotti
 218 et al., 2002b; Parteli et al., 2007; Franklin & Charru, 2011; Charru et al., 2013; Cour-
 219 rech du Pont, 2015), so that they also must be taken into account. For example, Khosronejad
 220 and Sotiropoulos (2017) showed that new barchans can be generated by a calving pro-
 221 cess on the horns of existing barchans, caused by the fluid shearing on the horn surface.
 222 Therefore, barchan collisions would be better described by the number of grains form-
 223 ing each pile, size and density of grains, flow strength and alignment of barchans, instead
 224 of only the mass ratio of piles and the offset parameter. Another aspect not investigated

225 in previous studies is the effect of initial conditions of bedforms on barchan collisions (tar-
 226 get barchan being initially a fully-developed barchan, a partially-developed barchan, or
 227 a conical pile). For the initial conditions, as well as the grain roundness, we did not ob-
 228 serve any significant difference in our experiments (see supporting information for snap-
 229 shots of barchan interactions with two conical piles as initial condition).

230 We propose that the short-range interaction patterns can be described by the off-
 231 set parameter, the Shields number, and the number of grains forming each pile. For the
 232 latter, the difference in the number of grains forming each pile, Δ_N , is proportional to
 233 the relative velocity of dunes, while the sum of those numbers, Σ_N , is proportional to
 234 the total size of the bedform once dunes have collided. We then introduce the dimen-
 235 sionless particle number:

$$\xi_N = \frac{\Delta_N}{\Sigma_N} \quad (1)$$

236 The Shields number is the ratio between mobile and resisting forces, linked to the
 237 fluid shearing and the grain weight, respectively, so that it takes into account the
 238 flow strength and the size and density of grains. Finally, the alignment of barchans
 239 is represented by the offset parameter σ (dimensionless), computed here as the
 240 transverse distance between the centroid of approaching barchans, η , divided by
 241 their average width: $\sigma = 2\eta/(W_U + W_D)$, where W_U and W_D are the widths of the
 242 upstream and downstream bedforms, respectively, and η is positive to the left of
 243 the target dune (with respect to the flow direction). Although we recognize three
 244 dimensionless groups, we decided to present all our data in two 2D maps in or-
 245 der to organize the patterns in the simplest and comprehensive way that we could
 246 find. Therefore, we plotted one interaction map for the aligned case (Figure 3a)
 247 and another one for the off-centered case (Figure 3b), where patterns are shown as
 248 functions of ξ_N and θ . In addition, for the off-centered case the map is parametrized
 249 by $\sigma < 0.5$ or $\sigma \geq 0.5$, which indicates if the the offset is relatively small or large,
 250 respectively. The number of grains forming each pile was considered as the ratio
 251 between the pile and grain masses.

252 Figures 3a and 3b show that the interaction patterns are relatively well organized
 253 by the ξ_N and θ groups, independent of the initial longitudinal separation between bed-
 254 forms, with transition regions between them where patterns are sometimes difficult to
 255 classify (their behavior in these regions is close to two patterns). Conscious of this dif-
 256 ficulty, we drew lines separating the different patterns, which we present in Figures 3c
 257 and 3d for the aligned and off-centered configurations, respectively. We drew such lines
 258 based solely on the experimental observations, and they consist in a tentative way to clas-
 259 sify the different patterns in θ vs. ξ_N maps. Although computation of those lines based
 260 on stability analyses or other analytical method remains to be done, we believe that the
 261 present maps may be useful for predicting the output of short-range barchan-barchan
 262 interactions under different conditions.

263 Based on image processing, we tracked the bedforms along the acquired images for
 264 each of the five patterns and identified some of their characteristic lengths. Because of
 265 approximately constant ratios between barchan dimensions (Hersen et al., 2002; Andreotti
 266 et al., 2002a), the projected area of a developed barchan multiplied by its height (around
 267 10% its width) is proportional to its volume, and, therefore, to its mass. However, in the
 268 present case barchans are being formed and deformed, interacting with each other, so
 269 that those relations are not completely valid. Conscious of that, we decided to analyze
 270 the projected areas of barchans as an indicator of the quantity of grains forming the dunes.
 271 Figure 3e presents the instantaneous values of the projected area of bedforms along time
 272 for the exchange pattern, and Figure 3f the evolution of the ratio between the lengths
 273 of the left and right horns (with respect to the flow direction), L_{hl} and L_{hr} , respectively.

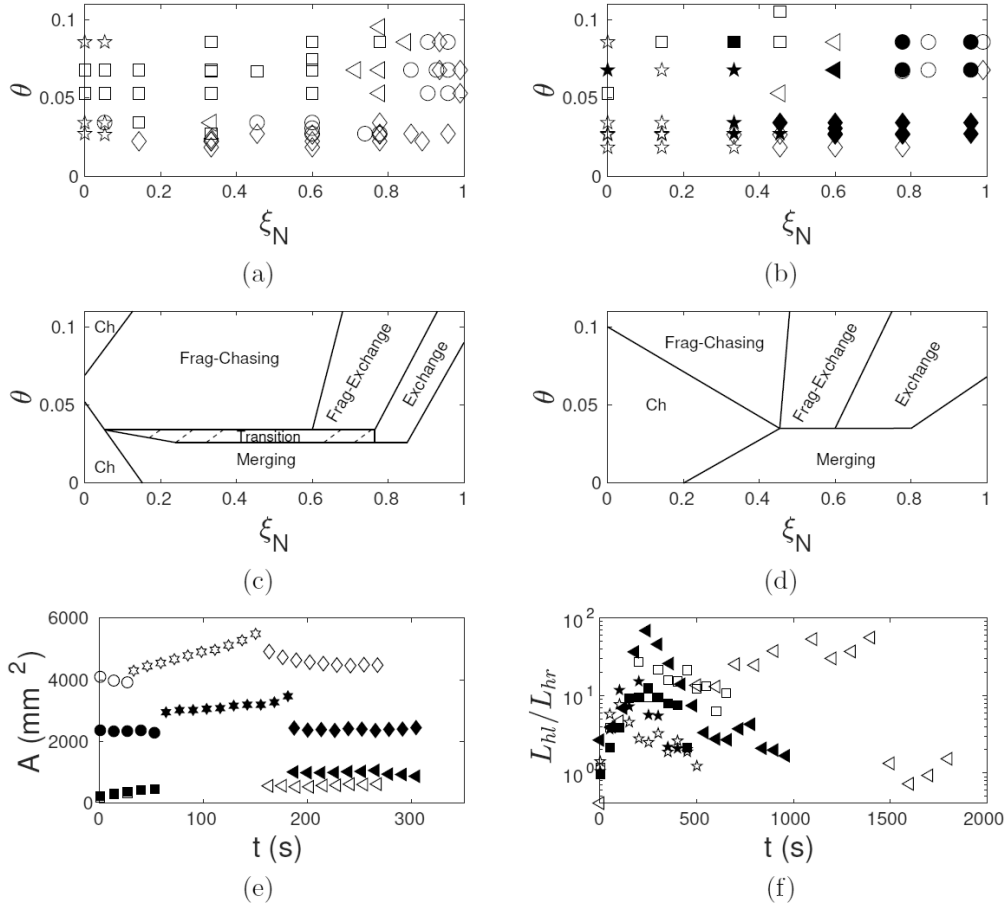


Figure 3. Figures (a) and (b): Patterns of barchan-barchan interactions as functions of ξ_N and θ for (a) aligned and (b) off-centered barchans. Stars, diamonds, circles, squares and triangles correspond to chasing, merging, exchange, fragmentation-chasing and fragmentation-exchange, respectively. In Figure (b), open symbols correspond to $\sigma < 0.5$ and solid symbols to $\sigma \geq 0.5$. Figures (c) and (d): Boundaries between different patterns for the aligned and off-centered barchans, respectively, where Ch stands for chasing and Frag to fragmentation. Figure (e): Area variation along time for the exchange pattern. Squares and circles correspond to the initial upstream (impact) and downstream (target) barchans, respectively, stars to the merged bedform, and diamonds and triangles to the merged bedform and new (expelled) barchan, respectively (tests 36 of Fig. S23 and 41 of Fig. S24 of the supporting information). Note that open squares are difficult to visualize in the graphic because they are at the same positions of solid squares. Fig (f): Ratio between the lengths of the left and right horns, L_{hl}/L_{hr} , of the downstream dune along time. Stars, squares and triangles correspond to chasing, fragmentation-chasing and fragmentation-exchange patterns, respectively (tests 61, 5 and 22 of Fig. S23, and 43, 31 and 5 of Fig. S24 of the supporting information). In Figs (e) and (f), open symbols correspond to the aligned and solid symbols to off-centered cases. All individual images that were processed to plot Figures (e) and (f) are available on Mendeley Data (<http://dx.doi.org/10.17632/jn3kt83hzh>)

274 We start by observing that the area of the upstream bedform increased in the be-
 275 ginning of all experiments because it was initially a conical pile, with a higher ratio be-
 276 tween its height and length, and, therefore, it spread out once the water flow was im-
 277 posed. While the upstream barchan was growing, the downstream one was already formed
 278 and lost grains by its horns without receiving much grains from the upstream bedform,
 279 so that its area decreased slightly in the beginning of each test. Figure 3e shows also that
 280 the area of the dune resulting from the collision increases along time due to its spread-
 281 ing, since just after collision the upstream dune (impact dune) climbs over the downstream
 282 one (target dune), as can be seen on movies available as supporting information. After
 283 that, a new born barchan is expelled with roughly the same area of the impact dune (see
 284 supporting information for a table showing the areas of impacting and expelled dunes
 285 of 15 tests). This indicates that the mass of the generated barchan is approximately that
 286 of the impacting one, though the constituent grains are not the same (Figures 1c and
 287 2c). Although this mass exchange of same value has been conjectured before (Vermeesch,
 288 2011), being even confounded with a solitary behavior in some cases (Schwämmle & Her-
 289 rmann, 2003), it had never been assessed from controlled experiments until now.

290 Finally, from Figure 3f we observe experimental evidence that the asymmetry of
 291 the downstream dune is large in wake-dominated processes (i.e., when the growth of one
 292 of the horns is due mainly to the fluid flow), the asymmetry being lower in the case of
 293 collision-generated asymmetries (not shown in Figure 3f, but presented in the support-
 294 ing information). This implies that the wake of upstream dunes (Palmer et al., 2012; Bris-
 295 tow et al., 2018), and not the collision itself, generates most of horns asymmetries. Al-
 296 though the origin of horns asymmetries has been studied previously (Parteli et al., 2014),
 297 it needs to be investigated further in the specific case of dune-dune interactions.

298 Although our experiments were limited to the subaqueous case, the resulting anal-
 299 ysis may be useful for predicting barchan-barchan interactions in other environments,
 300 such as Earth's deserts and on the surface of Mars. However, we expect differences re-
 301 lated to the larger quantities of grains involved in the aeolian and Martian dunes and,
 302 in particular, the trajectories followed by individual grains according to the state of the
 303 fluid. For the trajectories, grains move mainly by rolling and sliding and follow closely
 304 the fluid flow in the subaqueous case, being susceptible to small vortices and other small
 305 structures of the flow. This has been shown to be especially important for the grains mi-
 306 grating to the barchan horns (Alvarez & Franklin, 2018, 2019). When the fluid is a gas,
 307 grains move by saltation and reptation, and those in saltation follow basically a straight
 308 line in the main flow direction (Bagnold, 1941), being undisturbed by the small struc-
 309 tures of the flow. Discrepancies between the present analysis and the behavior in other
 310 environments are likely to occur, mainly for the wake-dominated processes, but where
 311 and when they occur, and to what extent, remain to be investigated.

312 4 Conclusions

313 In conclusion, subaqueous barchan-barchan interactions result in five different pat-
 314 terns for both aligned and off-centered configurations, being well organized in two maps
 315 as functions of ξ_N and θ and parametrized by σ . These maps provide a comprehensive
 316 and simple classification for the short-range interactions of subaqueous barchans and,
 317 although we have not analyzed the binary collisions in Earth's deserts and other plan-
 318 etary environments, given their long timescales, they may be useful for predicting the
 319 collisions of barchans in different environments. The present results represent a signif-
 320 icant step toward understanding the barcanoid forms, barchan asymmetries and size reg-
 321 ulation of barchans found in water, air, and other planetary environments.

322 **Acknowledgments**

323 W. R. Assis is grateful to FAPESP (grant no. 2019/10239-7), and E. M.
 324 Franklin is grateful to FAPESP (grant no. 2018/14981-7), to CNPq (grant no.
 325 400284/2016-2) and to FAEPEX/UNICAMP (grant no. 2112/19) for the financial
 326 support provided. Data supporting this work are available in the supporting infor-
 327 mation and in Mendeley Data (<http://dx.doi.org/10.17632/jn3kt83hzh>).

328 **References**

- 329 Alvarez, C. A., & Franklin, E. M. (2017, Dec). Birth of a subaqueous barchan
 330 dune. *Phys. Rev. E*, *96*, 062906. Retrieved from [https://link.aps.org/doi/](https://link.aps.org/doi/10.1103/PhysRevE.96.062906)
 331 [10.1103/PhysRevE.96.062906](https://link.aps.org/doi/10.1103/PhysRevE.96.062906) doi: 10.1103/PhysRevE.96.062906
- 332 Alvarez, C. A., & Franklin, E. M. (2018, Oct). Role of transverse displacements in
 333 the formation of subaqueous barchan dunes. *Phys. Rev. Lett.*, *121*, 164503. Re-
 334 trieved from <https://link.aps.org/doi/10.1103/PhysRevLett.121.164503>
 335 doi: 10.1103/PhysRevLett.121.164503
- 336 Alvarez, C. A., & Franklin, E. M. (2019, Oct). Horns of subaqueous barchan
 337 dunes: A study at the grain scale. *Phys. Rev. E*, *100*, 042904. Retrieved
 338 from <https://link.aps.org/doi/10.1103/PhysRevE.100.042904> doi:
 339 [10.1103/PhysRevE.100.042904](https://link.aps.org/doi/10.1103/PhysRevE.100.042904)
- 340 Andreotti, B., Claudin, P., & Douady, S. (2002a). Selection of dune shapes and
 341 velocities. part 1: Dynamics of sand, wind and barchans. *Eur. Phys. J. B*, *28*,
 342 321-329.
- 343 Andreotti, B., Claudin, P., & Douady, S. (2002b). Selection of dune shapes and ve-
 344 locities. part 2: A two-dimensional model. *Eur. Phys. J. B*, *28*, 341-352.
- 345 Bagnold, R. A. (1941). *The physics of blown sand and desert dunes*. London: Chap-
 346 man and Hall.
- 347 Bo, T. L., & Zheng, X. J. (2013). Collision behaviors of barchans in aeolian dune
 348 fields. *Environ. Earth. Sci.*, *70*, 2963-2970.
- 349 Bristow, N. R., Blois, G., Best, J. L., & Christensen, K. T. (2018). Turbulent flow
 350 structure associated with collision between laterally offset, fixed-bed barchan
 351 dunes. *J. Geophys. Res.-Earth*, *123*(9), 2157-2188.
- 352 Charru, F. (2006). Selection of the ripple length on a granular bed sheared by a liq-
 353 uid flow. *Phys. Fluids*, *18*(121508).
- 354 Charru, F., Andreotti, B., & Claudin, P. (2013). Sand ripples and dunes. *Ann. Rev.*
 355 *Fluid Mech.*, *45*(1), 469-493.
- 356 Claudin, P., & Andreotti, B. (2006). A scaling law for aeolian dunes on Mars,
 357 Venus, Earth, and for subaqueous ripples. *Earth Plan. Sci. Lett.*, *252*, 20-44.
- 358 Courrech du Pont, S. (2015). Dune morphodynamics. *C. R. Phys.*, *16*(1), 118 - 138.
- 359 Cúñez, F. D., Oliveira, G. V. G., & Franklin, E. M. (2018). Turbulent channel flow
 360 perturbed by triangular ripples. *J. Braz. Soc. Mech. Sci. Eng.*, *40*(138).
- 361 Durán, O., Schwämmle, V., & Herrmann, H. (2005, Aug). Breeding and solitary
 362 wave behavior of dunes. *Phys. Rev. E*, *72*, 021308. Retrieved from [https://](https://link.aps.org/doi/10.1103/PhysRevE.72.021308)
 363 link.aps.org/doi/10.1103/PhysRevE.72.021308 doi: 10.1103/PhysRevE
 364 .72.021308
- 365 Durán, O., Schwämmle, V., Lind, P. G., & Herrmann, H. (2009). The dune size dis-
 366 tribution and scaling relations of barchan dune fields. *Granular Matter*, *11*, 7-
 367 11.
- 368 Elbelrhiti, H., Claudin, P., & Andreotti, B. (2005). Field evidence for surface-wave-
 369 induced instability of sand dunes. *Nature*, *437*(04058).
- 370 Endo, N., Taniguchi, K., & Katsuki, A. (2004). Observation of the whole process
 371 of interaction between barchans by flume experiments. *Geophys. Res. Lett.*,
 372 *31*(12).

- 373 Franklin, E. M. (2015). Formation of sand ripples under a turbulent liquid flow.
374 *Appl. Math. Model.*, *39*(23), 7390-7400.
- 375 Franklin, E. M., & Charru, F. (2011). Subaqueous barchan dunes in turbulent shear
376 flow. Part 1. Dune motion. *J. Fluid Mech.*, *675*, 199-222.
- 377 Franklin, E. M., Figueiredo, F. T., & Rosa, E. S. (2014). The feedback effect caused
378 by bed load on a turbulent liquid flow. *J. Braz. Soc. Mech. Sci. Eng.*, *36*, 725-
379 736.
- 380 Gay, S. P. (1999). Observations regarding the movement of barchan sand dunes in
381 the nazca to tanaca area of southern peru. *Geomorphology*, *27*(3), 279 - 293.
- 382 G enois, M., du Pont, S. C., Hersen, P., & Gr egoire, G. (2013). An agent-based
383 model of dune interactions produces the emergence of patterns in deserts. *Geo-*
384 *phys. Res. Lett.*, *40*(15), 3909-3914.
- 385 G enois, M., Hersen, P., du Pont, S., & Gr egoire, G. (2013). Spatial structuring
386 and size selection as collective behaviours in an agent-based model for barchan
387 fields. *Eur. Phys. J. B*, *86*(447).
- 388 Herrmann, H. J., & Sauermann, G. (2000). The shape of dunes. *Physica A (Amster-*
389 *dam)*, *283*, 24-30.
- 390 Hersen, P. (2004). On the crescentic shape of barchan dunes. *Eur. Phys. J. B*,
391 *37*(4), 507-514.
- 392 Hersen, P., Andersen, K. H., Elbelrhiti, H., Andreotti, B., Claudin, P., & Douady,
393 S. (2004, Jan). Corridors of barchan dunes: Stability and size selection. *Phys.*
394 *Rev. E*, *69*, 011304. Retrieved from [https://link.aps.org/doi/10.1103/](https://link.aps.org/doi/10.1103/PhysRevE.69.011304)
395 [PhysRevE.69.011304](https://link.aps.org/doi/10.1103/PhysRevE.69.011304) doi: 10.1103/PhysRevE.69.011304
- 396 Hersen, P., & Douady, S. (2005). Collision of barchan dunes as a mechanism of size
397 regulation. *Geophys. Res. Lett.*, *32*(21).
- 398 Hersen, P., Douady, S., & Andreotti, B. (2002, Dec). Relevant length
399 scale of barchan dunes. *Phys. Rev. Lett.*, *89*, 264301. Retrieved from
400 <https://link.aps.org/doi/10.1103/PhysRevLett.89.264301> doi:
401 [10.1103/PhysRevLett.89.264301](https://link.aps.org/doi/10.1103/PhysRevLett.89.264301)
- 402 Hugenholtz, C. H., & Barchyn, T. E. (2012). Real barchan dune collisions and ejection
403 s. *Geophys. Res. Lett.*, *39*(2).
- 404 Katsuki, A., Kikuchi, M., Nishimori, H., Endo, N., & Taniguchi, K. (2011). Cellular
405 model for sand dunes with saltation, avalanche and strong erosion: collisional
406 simulation of barchans. *Earth Surf. Process. Landforms*, *36*(3), 372-382.
- 407 Katsuki, A., Nishimori, H., Endo, N., & Taniguchi, K. (2005). Collision dynamics of
408 two barchan dunes simulated using a simple model. *J. Phys. Soc. Jpn.*, *74*(2),
409 538-541.
- 410 Khosronejad, A., & Sotiropoulos, F. (2017). On the genesis and evolution of barchan
411 dunes: morphodynamics. *J. Fluid Mech.*, *815*, 117-148.
- 412 Kocurek, G., Ewing, R. C., & Mohrig, D. (2010). How do bedform patterns arise?
413 new views on the role of bedform interactions within a set of boundary condi-
414 tions. *Earth Surf. Process. Landforms*, *35*(1), 51-63.
- 415 Norris, R. M., & Norris, K. S. (1961). Algodones Dunes of Southeastern California.
416 *GSA Bulletin*, *72*(4), 605-619.
- 417 Palmer, J. A., Mejia-Alvarez, R., Best, J. L., & Christensen, K. T. (2012). Particle-
418 image velocimetry measurements of flow over interacting barchan dunes. *Exp.*
419 *Fluids*, *52*, 809-829.
- 420 Parteli, E. J. R., Dur an, O., Bourke, M. C., Tsoar, H., P oschel, T., & Herrmann,
421 H. (2014). Origins of barchan dune asymmetry: Insights from numerical
422 simulations. *Aeol. Res.*, *12*, 121-133.
- 423 Parteli, E. J. R., Dur an, O., & Herrmann, H. J. (2007, Jan). Minimal size of a
424 barchan dune. *Phys. Rev. E*, *75*, 011301. Retrieved from [https://link.aps](https://link.aps.org/doi/10.1103/PhysRevE.75.011301)
425 [.org/doi/10.1103/PhysRevE.75.011301](https://link.aps.org/doi/10.1103/PhysRevE.75.011301) doi: 10.1103/PhysRevE.75.011301
- 426 Parteli, E. J. R., & Herrmann, H. J. (2007, Oct). Dune formation on the present
427 mars. *Phys. Rev. E*, *76*, 041307. Retrieved from <https://link.aps.org/doi/>

- 428 10.1103/PhysRevE.76.041307 doi: 10.1103/PhysRevE.76.041307
429 Schlichting, H. (2000). *Boundary-layer theory*. New York: Springer.
430 Schwämmle, V., & Herrmann, H. J. (2003). Solitary wave behaviour of sand dunes.
431 *Nature*, *426*, 619-620.
432 Vermeesch, P. (2011). Solitary wave behavior in sand dunes observed from space.
433 *Geophys. Res. Lett.*, *38*(22).
434 Zhou, X., Wang, Y., & Yang, B. (2019). Three-dimensional numerical simulations of
435 barchan dune interactions in unidirectional flow. *Particul. Sci. Technol.*, *37*(7),
436 835-842.

Supporting Information for “A comprehensive picture for binary interactions of subaqueous barchans”

W. R. Assis¹, E. M. Franklin²

^{1,2}School of Mechanical Engineering, UNICAMP - University of Campinas,

Rua Mendeleev, 200, Campinas, SP, Brazil

Contents of this file

1. Figures S1 to S25
2. Tables S1 and S2

Additional Supporting Information (Files uploaded separately)

1. Captions for Movies S1 to S10

Introduction

This supporting information presents the layout of the experimental device, a photograph of the test section, microscopy images of the used grains, lists of the tested conditions, snapshots of barchan interactions with different initial conditions and grain types, additional graphics, and movies showing examples of each collision pattern. We note that

all individual images that were processed to plot Figs. 3e and 3f of the paper are available on Mendeley Data (<http://dx.doi.org/10.17632/jn3kt83hzh>).

The experiments described in the paper were conducted in a water channel of transparent material, for which the layout and a photograph of the test section are shown in Figs. S1 and S2, respectively. With the channel previously filled with water, controlled grains were poured inside, forming a pair of bedforms in either aligned or off-centered configurations. By imposing a water flow, each bedform was deformed into a barchan shape and interacted with each other.

A camera of complementary metal-oxide-semiconductor (CMOS) type was placed above the channel in order to acquire images of the bedforms. The camera resolution was of $1920 \text{ px} \times 1080 \text{ px}$ at 60 Hz and it was mounted on a traveling system, both controlled by a computer. Depending on the tested conditions, the region of interest (ROI) was set to $1920 \text{ px} \times 701 \text{ px}$ or to $1920 \text{ px} \times 801 \text{ px}$, and the frequency to 30 Hz. We used a lens of 60 mm focal distance and F2.8 maximum aperture mounted on the camera, and lamps of light-emitting diode (LED) were branched to a continuous-current source to provide the necessary light. The conversion from px to a physical system of units was made by means of a scale placed in the channel previously filled with water. The acquired images were processed by numerical scripts written in the course of this work. They basically removed the image background, binarized the images, and identified the main morphological properties of barchans and their relative distances.

Two observations are made just below concerning imperfections in our data on dune-dune interaction.

OBS1: in Fig.S23 (below), test runs 1, 2, 3, 29, 33, 34 and 37 were in the frontier between the exchange and merging patterns, the resulting quantity of ejected grains being so small that the ejected bedform spread out as soon as it was ejected. We classified these experimental points as exchange, but we understand that they could have been classified as merging as well.

OBS2: in Fig.S23 (below), the image recordings of test runs 24 and 44 were interrupted just before the end of the interaction process between barchans. This happened because the translation mechanism arrived at its end position. However, we observed that in both cases the interaction pattern was the fragmentation-chasing one (which can also be guessed from the respective movies).

Concerning the water flow, experiments with particle image velocimetry (PIV) were performed in the test section of the channel in the absence of grains, and they are described in detail in previous works cited in the paper. For the PIV experiments, a laser sheet was positioned in the vertical plane of symmetry of the channel, and a charge-coupled device (CCD) camera was placed orthogonally to that sheet. Different flow rates were then imposed in the channel without the presence of grains (mono-phase water flow). The laser was of dual-cavity Nd:YAG Q-switched type capable to emit 2×130 mJ at a maximum pulse rate of 15 Hz and the camera sensor had a size of $7.4 \mu\text{m} \times 7.4 \mu\text{m}$ (px^2), with a spatial resolution of $2048 \text{ px} \times 2048 \text{ px}$. When synchronized, the camera and laser were operated at 4 Hz for the acquisition of image pairs, and the time between frames was adjusted in accordance with the flow velocities. We employed hollow glass beads 10

μm in diameter with a specific gravity of 1.05 as seeding particles, and the magnification was of approximately 0.1.

We obtained profiles following closely the law of the wall, $u^+ = 1/\kappa \ln y^+ + B$, where u^+ is the mean velocity normalized by the shear velocity u_* , $\kappa = 0.41$ is the von Kármán constant, $y^+ = y\nu/u_*$ is the vertical coordinate normalized by the viscous length, ν is the kinematic viscosity and B is a constant. An example of measured profile is given in Fig. S10, which follows a hydraulic smooth regime. From the profile inclination, we found the experimental values of u_* and Darcy friction factor f . The latter was then compared with the friction factor obtained from the Blasius correlation, $f_{bla} = 0.316Re_{dh}^{-1/4}$, where $Re_{dh} = Ud_h/\nu$ is the Reynolds number based on the hydraulic diameter, U being the cross-sectional mean velocity and $d_h = 3.05 \delta$ (d_h is the cross-sectional area multiplied by four and divided by the cross-sectional perimeter). Table S1 presents the values of U , u_* , f and f_{bla} obtained for the bottom wall of the channel for each Reynolds number. From Tab. S1, we observe that differences between the experimental and correlated friction factors are equal or less than 6 % (proportional to u_*^2 , and then to the Shields number), implying differences in u_* of less than 3 %.

Movie S1. Chasing_Align.gif Movie showing an example of the chasing pattern in aligned configuration

Movie S2. Chasing_Stag.gif Movie showing an example of the chasing pattern in off-centered configuration

Movie S3. Merging_Align.gif Movie showing an example of the merging pattern in aligned configuration

Movie S4. Merging_Stag.gif Movie showing an example of the merging pattern in off-centered configuration

Movie S5. Exchange_Align.gif Movie showing an example of the exchange pattern in aligned configuration

Movie S6. Exchange_Stag.gif Movie showing an example of the exchange pattern in off-centered configuration

Movie S7. Fragmentation_Chasing_Align.gif Movie showing an example of the fragmentation-chasing pattern in aligned configuration

Movie S8. Fragmentation_Chasing_Stag.gif Movie showing an example of the fragmentation-chasing pattern in off-centered configuration

Movie S9. Fragmentation_Exchange_Align.gif Movie showing an example of the fragmentation-exchange pattern in aligned configuration

Movie S10. Fragmentation_Exchange_Stag.gif Movie showing an example of the fragmentation-exchange pattern in off-centered configuration

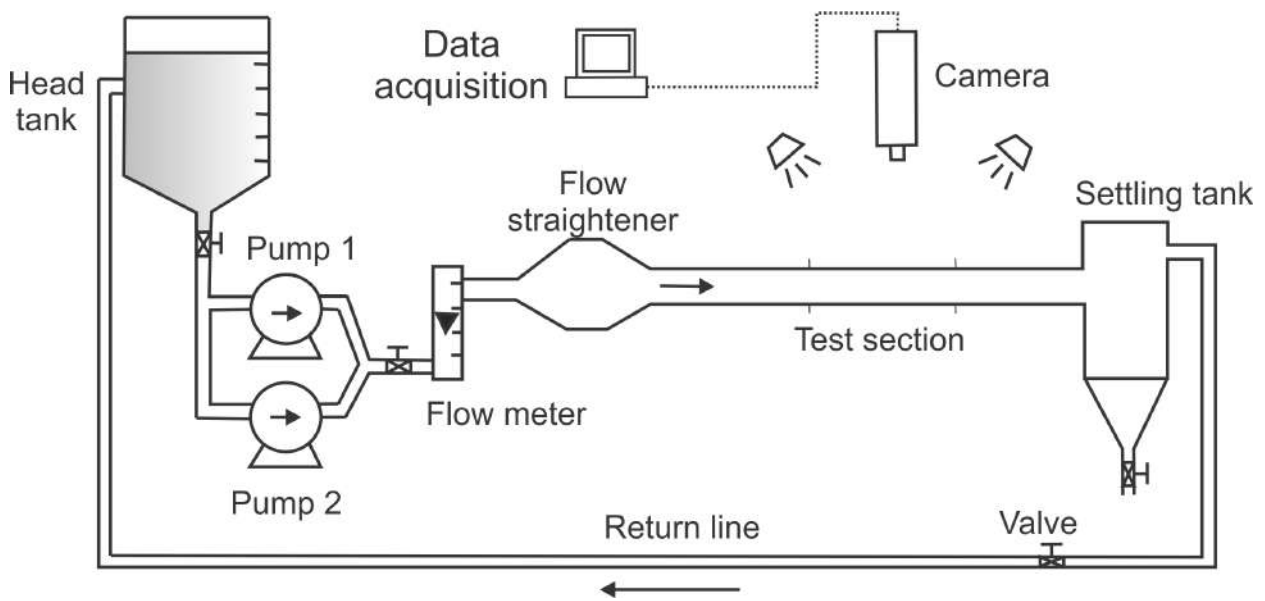


Figure S1. Layout of the experimental setup.

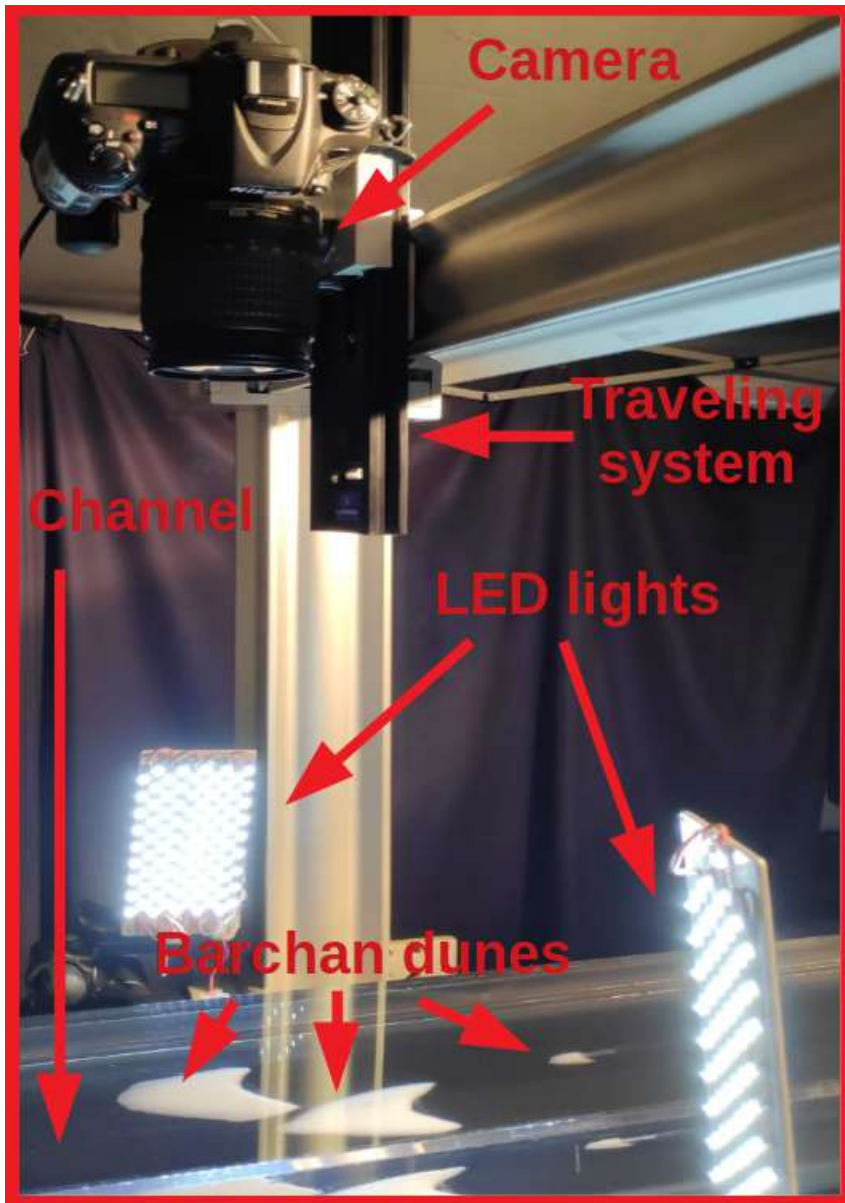


Figure S2. Photograph of the test section.

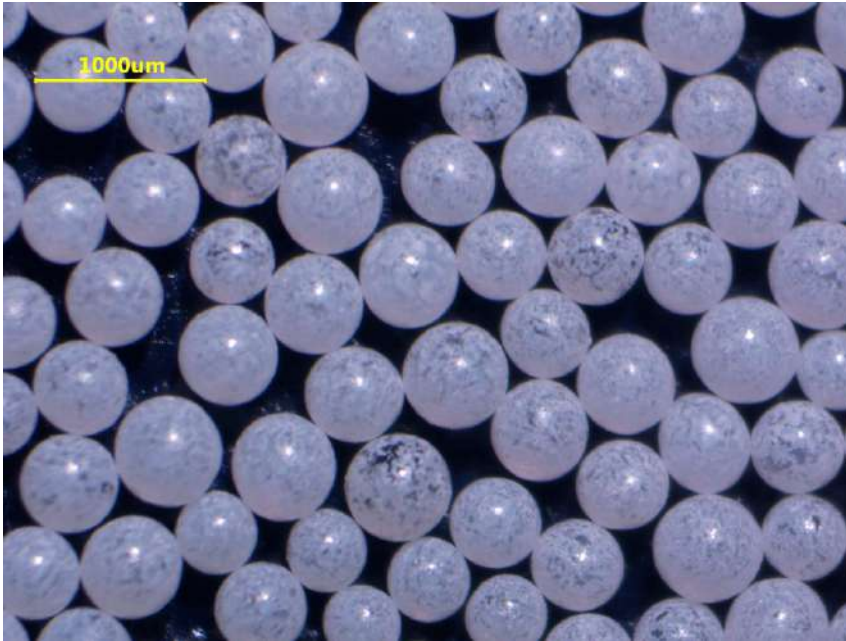


Figure S3. Microscopy image for the $0.40 \text{ mm} \leq d \leq 0.60 \text{ mm}$ round glass beads of white color.



Figure S4. Microscopy image for the $0.40 \text{ mm} \leq d \leq 0.60 \text{ mm}$ round glass beads of red color.

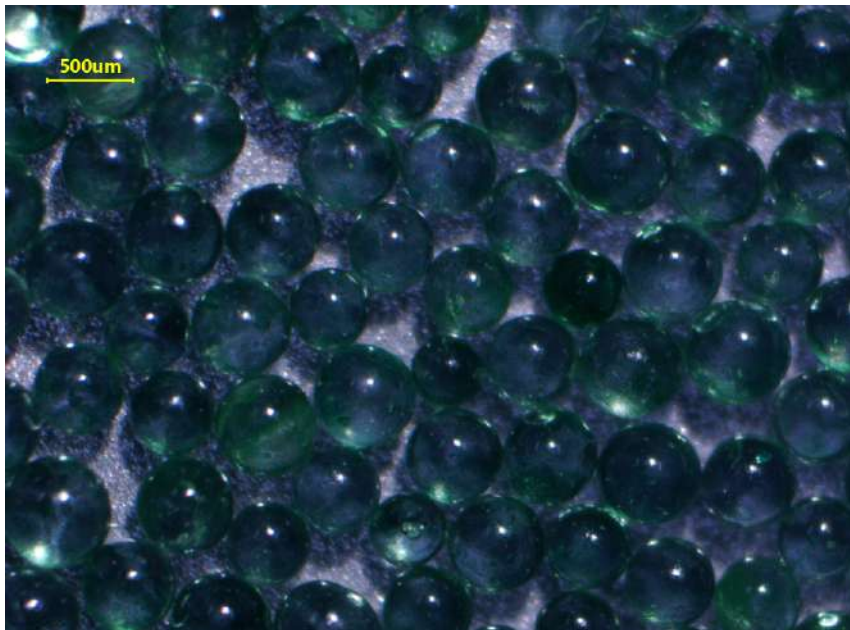


Figure S5. Microscopy image for the $0.40 \text{ mm} \leq d \leq 0.60 \text{ mm}$ round glass beads of green color.

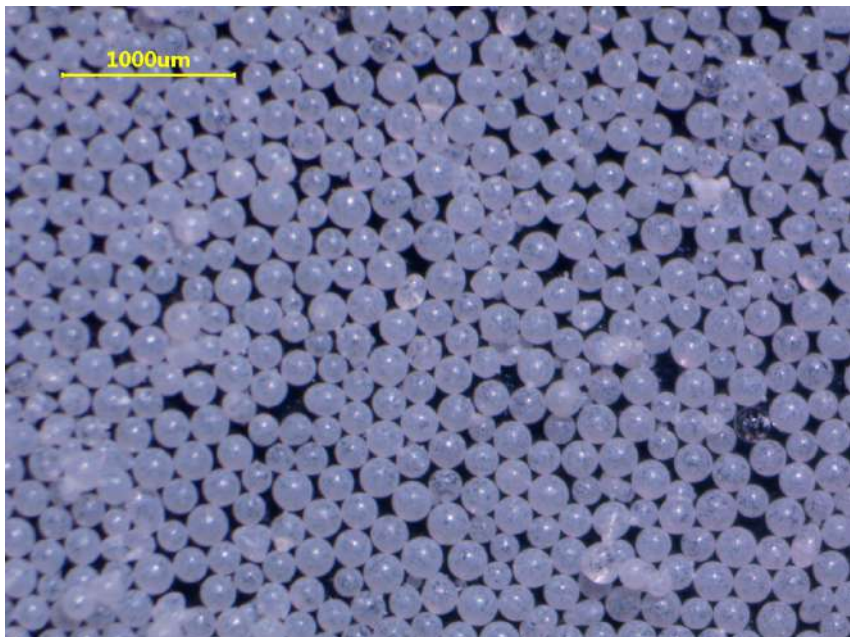


Figure S6. Microscopy image for the $0.15 \text{ mm} \leq d \leq 0.25 \text{ mm}$ round glass beads of white color.

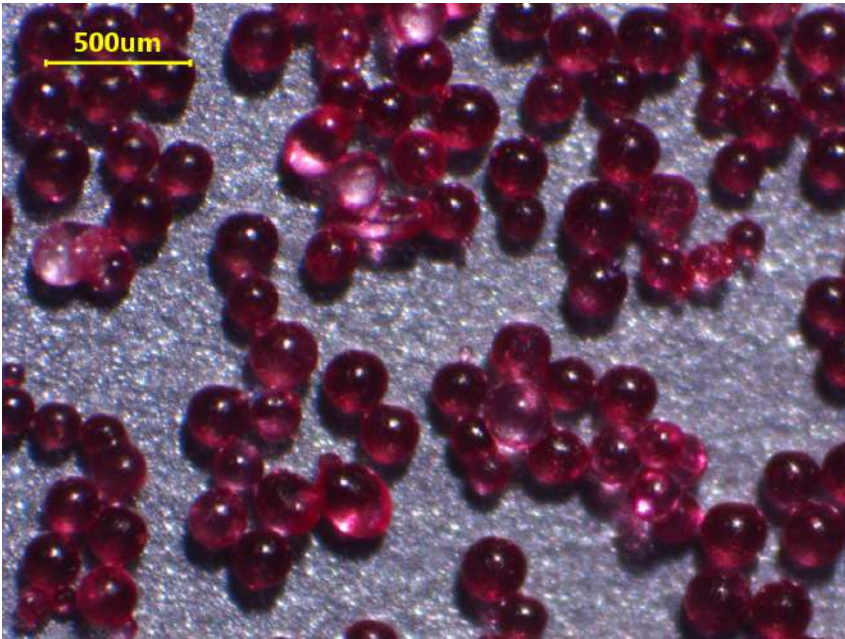


Figure S7. Microscopy image for the $0.15 \text{ mm} \leq d \leq 0.25 \text{ mm}$ round glass beads of red color.

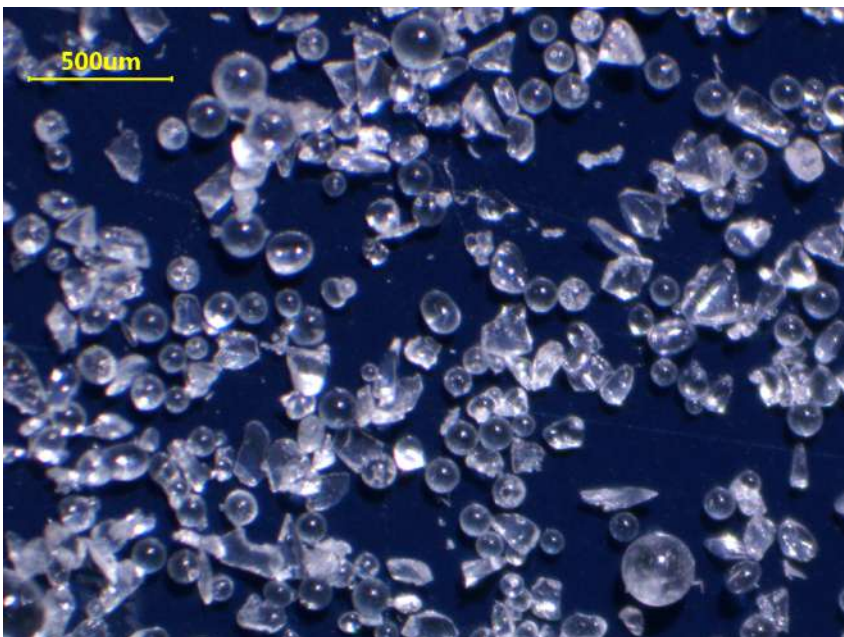


Figure S8. Microscopy image for the $0.21 \text{ mm} \leq d \leq 0.30 \text{ mm}$ angular glass beads.

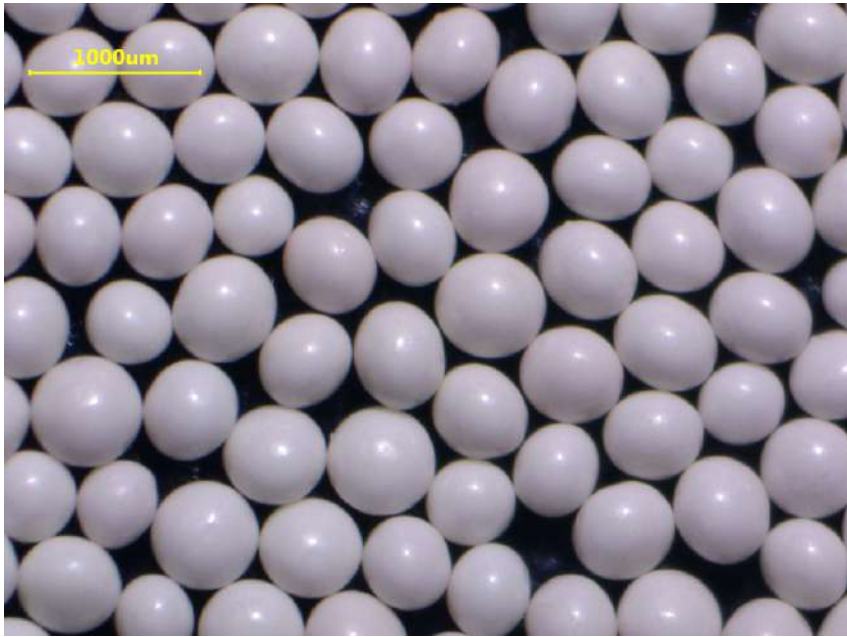


Figure S9. Microscopy image for the $0.40 \text{ mm} \leq d \leq 0.60 \text{ mm}$ round zirconium beads.

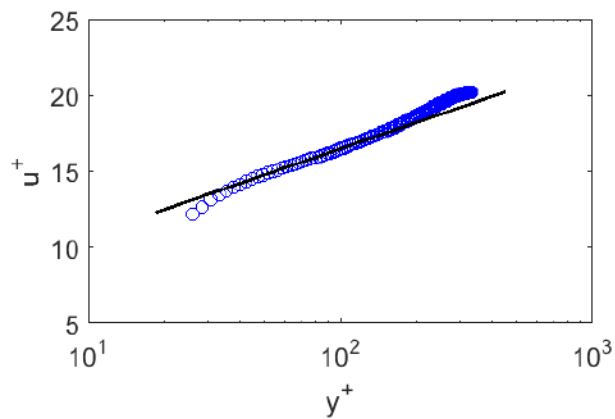
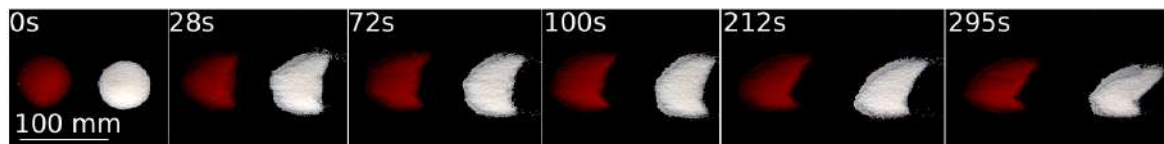
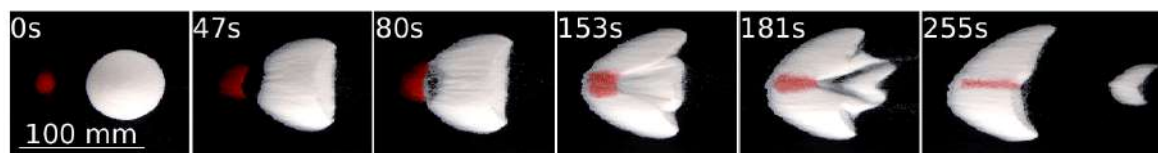


Figure S10. Velocity profile over the bottom wall of the channel in log-normal scales. Circles correspond to experimental points and the continuous line to the inclination of the logarithmic region.



(a)

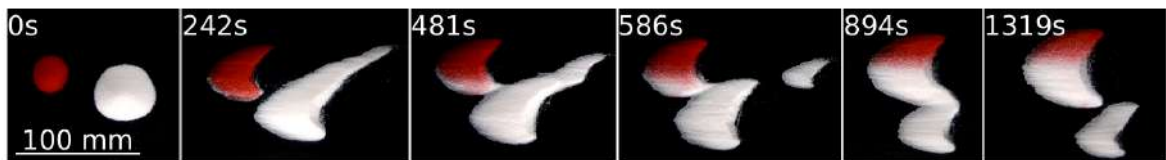


(b)

Figure S11. Snapshots of barchan interactions for aligned dunes, with two conical piles as initial condition. In the snapshots, the water flow is from left to right, the upstream pile consisting of red (darker) glass beads and the downstream pile of white (clearer) glass beads. In Fig. (a), $0.40 \text{ mm} \leq d \leq 0.60 \text{ mm}$, in Fig. (b) $0.15 \text{ mm} \leq d \leq 0.25 \text{ mm}$, and the corresponding times are shown in each frame. (a) Chasing, equivalent to test 61 of Fig. S23, but with two initial conical piles; (b) exchange, equivalent to test 36 of Fig. S23, but with two initial conical piles.

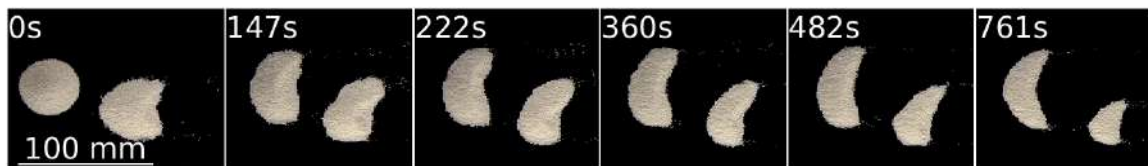


(a)

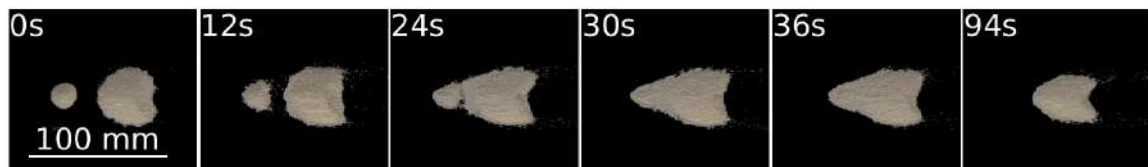


(b)

Figure S12. Snapshots of barchan interactions for off-centered dunes, with two conical piles as initial condition. In the snapshots, the water flow is from left to right, the upstream pile consisting of red (darker) glass beads and the downstream pile of white (clearer) glass beads. In Fig. (a), $0.40 \text{ mm} \leq d \leq 0.60 \text{ mm}$, in Fig. (b) $0.15 \text{ mm} \leq d \leq 0.25 \text{ mm}$, and the corresponding times are shown in each frame. (a) Merging (test 14 of Fig. S24); (b) fragmentation-exchange, equivalent to test 5 of Fig. S24, but with two initial conical piles.

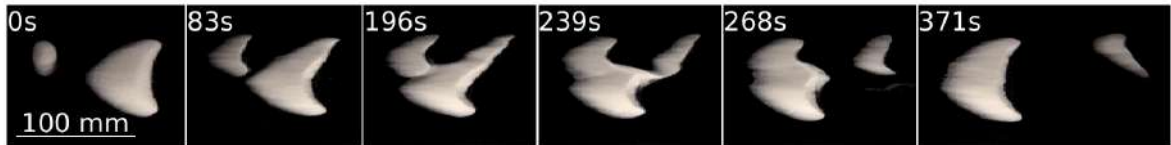


(a)

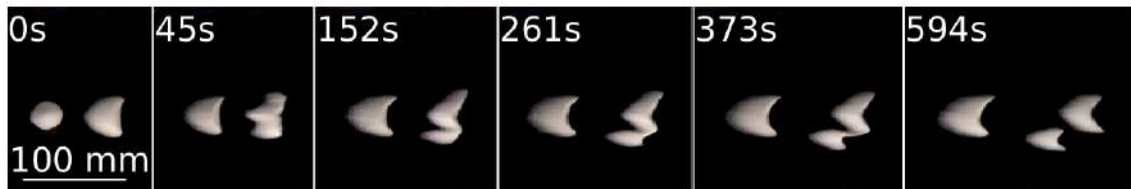


(b)

Figure S13. Snapshots of barchan interactions for off-centered and aligned dunes consisting of zirconium beads with $0.40 \text{ mm} \leq d \leq 0.60$. In the snapshots, the water flow is from left to right, and the corresponding times are shown in each frame. (a) Chasing (off-centered, test 47 of Fig. S24); (b) merging (aligned, test 27 of Fig. S23).

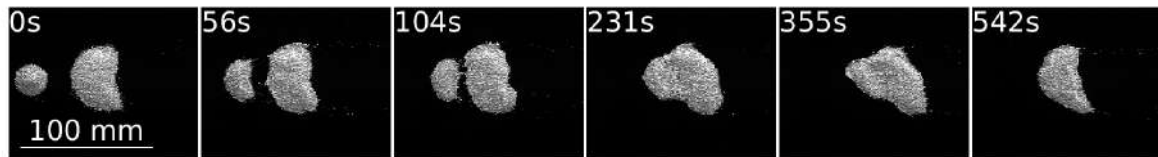


(a)

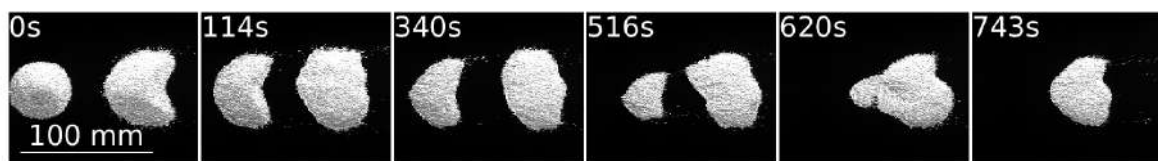


(b)

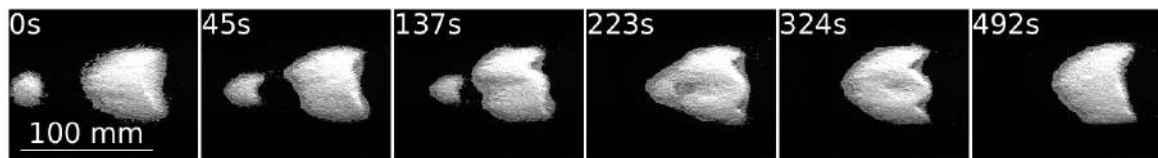
Figure S14. Snapshots of barchan interactions for off-centered and aligned dunes consisting of angular glass beads with $0.21 \text{ mm} \leq d \leq 0.30 \text{ mm}$. In the snapshots, the water flow is from left to right, and the corresponding times are shown in each frame. (a) Exchange (off-centered, test 18 of Fig. S24); (b) fragmentation-chasing (aligned, test 63 of Fig. S23).



(a)



(b)



(c)

Figure S15. Snapshots of merging patterns for aligned dunes. In the snapshots, the water flow is from left to right, and the corresponding times are shown in each frame. (a) and (b) Zirconium beads with $0.40 \text{ mm} \leq d \leq 0.60$ (tests 8 and 41 of Fig. S23, respectively); (c) glass beads with $0.40 \text{ mm} \leq d \leq 0.60 \text{ mm}$ (test 20 of Fig. S23).

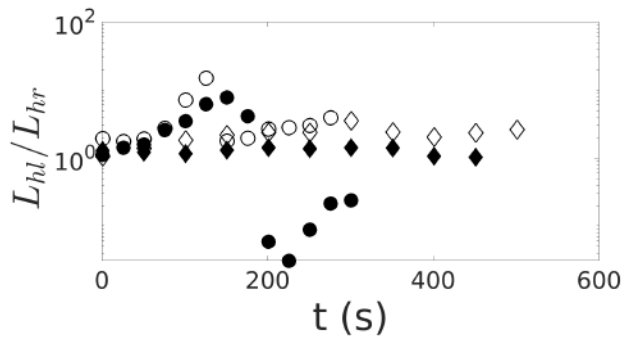


Figure S16. Ratio between the lengths of the left and right horns, L_{hl}/L_{hr} , of the downstream dune along time. Diamonds and circles correspond to the merging and exchange patterns, respectively. Open symbols correspond to the aligned and solid symbols to off-centered cases (they correspond to tests 65 and 36 of Fig. S23, and 38 and 41 of Fig. S24).

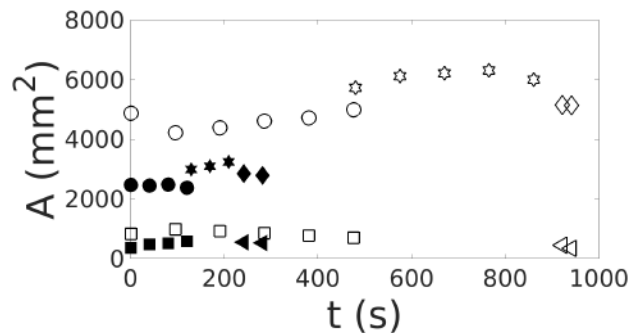


Figure S17. Area variation along time for the exchange pattern. Squares and circles correspond to the initial upstream (impact) and downstream (target) barchans, respectively, stars to the merged bedform, and diamonds and triangles to the merged bedform and new (expelled) barchan, respectively. Open symbols correspond to the aligned and solid symbols to off-centered cases (tests 38 of Fig. S23 and 18 of Fig. S24).

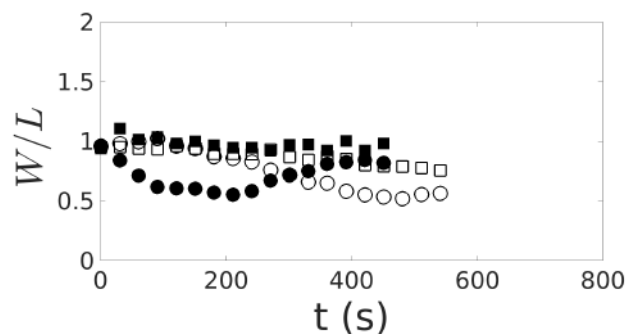


Figure S18. Evolution of W/L along time for the chasing pattern. Squares and circles correspond to the initial upstream (impact) and downstream (target) barchans, respectively. Open symbols correspond to the aligned and solid symbols to off-centered cases (tests 61 of Fig. S23 and 43 of Fig. S24).

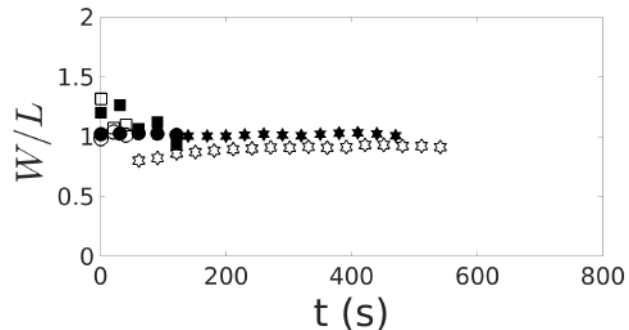


Figure S19. Evolution of W/L along time for the merging pattern. Squares and circles correspond to the initial upstream (impact) and downstream (target) barchans, respectively, and stars to the merged bedform. Open symbols correspond to the aligned and solid symbols to off-centered cases (tests 65 of Fig. S23 and 38 of Fig. S24).

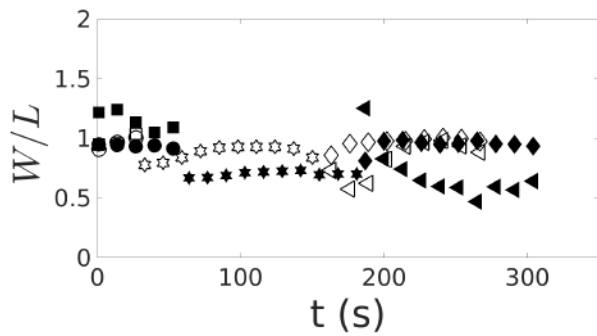


Figure S20. Evolution of W/L along time for the exchange pattern. Squares and circles correspond to the initial upstream (impact) and downstream (target) barchans, respectively, stars to the merged bedform, and diamonds and triangles to the merged bedform and new (expelled) barchan, respectively. Open symbols correspond to the aligned and solid symbols to off-centered cases (tests 36 of Fig. S23 and 41 of Fig. S24).

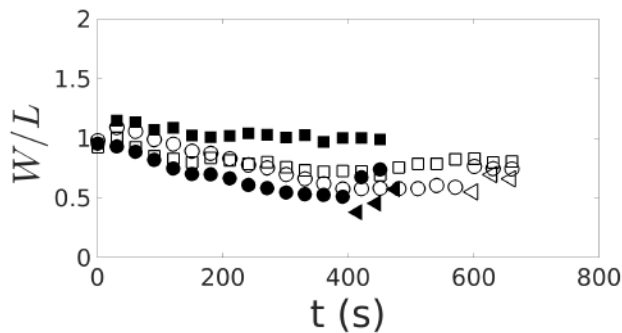


Figure S21. Evolution of W/L along time for the fragmentation-chasing pattern. Squares and circles correspond to the initial upstream (impact) and downstream (target) barchans, respectively, and triangles to the new (expelled) barchan, respectively. Open symbols correspond to the aligned and solid symbols to off-centered cases (tests 5 of Fig. S23 and 31 of Fig. S24).

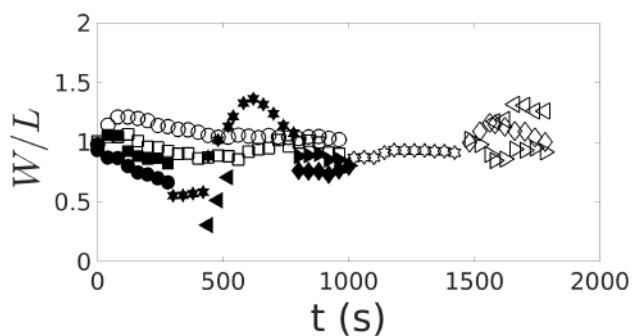


Figure S22. Evolution of W/L along time for the fragmentation-exchange pattern. Squares and circles correspond to the initial upstream (impact) and downstream (target) barchans, respectively, stars to the merged bedform, diamonds and right triangles to upstream and downstream bedforms generated by the split of the merged barchan, respectively, and left triangles to the new (expelled) barchan (“baby” barchan). Open symbols correspond to the aligned and solid symbols to off-centered cases (tests 22 of Fig. S23 and 5 of Fig. S24).

Aligned position															
#	η	σ	$\Delta x_b/D$	$\Delta x_c/D$	m_i	m_t	N_i	N_t	ξ_N	ρ_s	d	u	Re.	θ	Pattern
-	(mm)	-	-	-	(g)	(g)	-	-	-	(kg/m ³)	(mm)	(m/s)	-	-	-
1	-3	-0.07	0.97	2.83	2.0	8.0	12223	48892	0.60	2500	0.50	0.0141	7	0.027	Exchange
2	-2	-0.04	0.82	2.56	2.0	8.0	12223	48892	0.60	2500	0.50	0.0150	8	0.031	Exchange
3	-2	-0.04	0.68	2.48	2.0	8.0	12223	48892	0.60	2500	0.50	0.0159	8	0.034	Exchange
4	-5	-0.12	0.66	2.34	2.0	8.0	190986	763944	0.60	2500	0.20	0.0141	3	0.068	Frag-Chasing
5	2	0.05	0.73	2.43	2.0	8.0	190986	763944	0.60	2500	0.20	0.0159	3	0.086	Frag-Chasing
6	0	-0.01	1.01	2.66	2.0	8.0	91069	364277	0.60	2500	0.26	0.0141	4	0.053	Frag-Chasing
7	-2	-0.05	0.80	2.46	2.0	8.0	91069	364277	0.60	2500	0.26	0.0168	4	0.075	Frag-Chasing
8	-1	-0.03	0.77	2.14	2.0	8.0	7453	29812	0.60	4100	0.50	0.0168	8	0.019	Merging
9	-3	-0.07	0.79	2.21	2.0	8.0	7453	29812	0.60	4100	0.50	0.0185	9	0.022	Merging
10	0	0.00	1.05	2.50	2.0	8.0	7453	29812	0.60	4100	0.50	0.0202	10	0.026	Merging
11	2	0.03	0.70	2.14	4.0	8.0	24446	48892	0.33	2500	0.50	0.0141	7	0.027	Frag-Chasing
12	2	0.05	0.60	2.07	4.0	8.0	24446	48892	0.33	2500	0.50	0.0159	8	0.034	Frag-Exchange
13	1	0.03	0.80	2.01	4.0	8.0	381972	763944	0.33	2500	0.20	0.0141	3	0.068	Frag-Chasing
14	-1	-0.01	0.74	1.93	4.0	8.0	381972	763944	0.33	2500	0.20	0.0159	3	0.086	Frag-Chasing
15	1	0.02	0.67	2.15	4.0	8.0	182138	364277	0.33	2500	0.26	0.0141	4	0.053	Frag-Chasing
16	2	0.05	0.74	2.12	4.0	8.0	182138	364277	0.33	2500	0.26	0.0159	4	0.067	Frag-Chasing
17	4	0.09	0.75	1.99	4.0	8.0	14906	29812	0.33	4100	0.50	0.0168	8	0.019	Merging
18	1	0.03	0.50	1.68	4.0	8.0	14906	29812	0.33	4100	0.50	0.0185	9	0.022	Merging
19	-3	-0.05	0.52	1.72	8.0	16.0	29812	59624	0.33	4100	0.50	0.0185	9	0.022	Merging
20	-5	-0.11	1.13	3.11	1.0	8.0	6112	48892	0.78	2500	0.50	0.0141	7	0.027	Merging
21	-3	-0.06	1.18	3.26	1.0	8.0	6112	48892	0.78	2500	0.50	0.0159	8	0.034	Merging
22	0	0.00	0.76	2.75	1.0	8.0	95493	763944	0.78	2500	0.20	0.0141	3	0.068	Frag-Exchange
23	-3	-0.08	1.02	3.03	1.0	8.0	95493	763944	0.78	2500	0.20	0.0159	3	0.086	Frag-Chasing
24	-3	-0.08	0.83	2.76	1.0	8.0	95493	763944	0.78	2500	0.20	0.0168	3	0.096	Frag-Exchange
25	-5	-0.14	0.84	2.66	1.0	8.0	45535	364277	0.78	2500	0.26	0.0141	4	0.053	Frag-Exchange
26	1	0.03	1.14	2.58	1.0	8.0	3727	29812	0.78	4100	0.50	0.0185	9	0.022	Merging
27	1	0.04	0.77	2.45	1.0	8.0	3727	29812	0.78	4100	0.50	0.0202	10	0.027	Merging
28	0	0.00	0.51	2.02	3.0	8.0	18335	48892	0.45	2500	0.50	0.0141	7	0.027	Merging
29	-3	-0.06	0.47	1.99	3.0	8.0	18335	48892	0.45	2500	0.50	0.0159	8	0.034	Exchange
30	-1	-0.02	1.51	4.67	0.3	14.0	1833	85562	0.96	2500	0.50	0.0141	7	0.027	Merging
31	-4	-0.17	1.44	4.35	0.1	3.0	9549	286479	0.94	2500	0.20	0.0141	3	0.068	Merging
32	-3	-0.11	1.12	3.77	0.1	3.0	9549	286479	0.94	2500	0.20	0.0159	3	0.086	Merging
33	-3	-0.06	1.39	4.24	0.3	14.0	28648	1336902	0.96	2500	0.20	0.0141	3	0.068	Exchange
34	-2	-0.06	1.42	4.15	0.3	8.0	28648	763944	0.93	2500	0.20	0.0141	3	0.068	Exchange
35	-5	-0.15	1.25	3.64	0.3	4.0	28648	381972	0.86	2500	0.20	0.0141	3	0.068	Exchange
36	2	0.04	1.01	4.48	0.3	14.0	28648	1336902	0.96	2500	0.20	0.0159	3	0.086	Exchange
37	0	0.01	1.38	4.09	0.3	14.0	13660	637484	0.96	2500	0.26	0.0141	4	0.053	Exchange
38	-7	-0.13	0.65	2.75	2.0	16.0	12223	97785	0.78	2500	0.50	0.0141	7	0.027	Exchange
39	-4	-0.07	0.53	2.34	3.0	20.0	18335	122231	0.74	2500	0.50	0.0141	7	0.027	Exchange
40	0	0.01	0.71	2.59	3.0	18.0	286479	1718873	0.71	2500	0.20	0.0141	3	0.068	Frag-Exchange
41	-2	-0.03	0.54	1.76	12.0	16.0	44719	59624	0.14	4100	0.50	0.0185	9	0.022	Merging
42	-3	-0.09	0.83	2.79	0.5	6.0	47746	572958	0.85	2500	0.20	0.0159	3	0.086	Frag-Exchange
43	-3	-0.08	1.13	3.51	0.3	6.0	28648	572958	0.90	2500	0.20	0.0159	3	0.086	Exchange
44	-5	-0.15	1.45	3.92	0.3	6.0	13660	273208	0.90	2500	0.26	0.0141	4	0.053	Exchange
45	-4	-0.10	2.18	6.33	0.1	20.0	4553	910692	0.99	2500	0.26	0.0141	4	0.053	Merging
46	-3	-0.10	0.63	1.95	1.5	2.0	68302	91069	0.14	2500	0.26	0.0141	4	0.053	Frag-Chasing
47	-1	-0.03	0.65	1.80	3.0	3.0	136604	136604	0.00	2500	0.26	0.0141	4	0.053	Frag-Chasing
48	-3	-0.09	0.68	2.14	1.5	4.0	68302	182138	0.45	2500	0.26	0.0159	4	0.067	Frag-Chasing
49	-1	-0.01	0.46	1.70	2.0	4.0	12223	24446	0.33	2500	0.50	0.0133	7	0.024	Merging
50	-3	-0.07	0.94	3.11	0.6	8.0	3667	48892	0.86	2500	0.50	0.0141	7	0.027	Merging

August 19, 2020, 7:05pm

Aligned position – Continuation															
#	η	σ	$\Delta x_b/D$	$\Delta x_c/D$	m_i	m_t	N_i	N_t	ξ_N	ρ_s	d	u_*	Re_*	θ	<i>Pattern</i>
-	(mm)	-	-	-	(g)	(g)	-	-	-	(kg/m ³)	(mm)	(m/s)	-	-	-
51	0	-0.01	0.92	2.83	0.7	12.0	2609	44719	0.89	4100	0.50	0.0185	9	0.022	Merging
52	-1	-0.04	0.59	1.94	1.5	2.0	143239	190986	0.14	2500	0.20	0.0141	3	0.068	Frag-Chasing
53	0	-0.01	0.50	1.71	3.0	3.0	286479	286479	0.00	2500	0.20	0.0159	3	0.086	Chasing
54	0	0.01	0.22	1.40	9.0	10.0	33539	37266	0.05	4100	0.50	0.0202	10	0.027	Chasing
55	1	0.01	0.45	1.76	10.0	10.0	61115	61115	0.00	2500	0.50	0.0141	7	0.027	Chasing
56	2	0.04	0.38	1.67	9.0	10.0	55004	61115	0.05	2500	0.50	0.0159	8	0.034	Exchange
57	0	-0.01	0.59	1.79	2.7	3.0	257831	286479	0.05	2500	0.20	0.0141	3	0.068	Frag-Chasing
58	0	0.01	0.65	1.90	2.7	3.0	257831	286479	0.05	2500	0.20	0.0159	3	0.086	Chasing
59	2	0.04	0.48	1.71	3.0	3.0	286479	286479	0.00	2500	0.20	0.0141	3	0.068	Frag-Chasing
60	1	0.03	0.58	1.91	2.7	3.0	16501	18335	0.05	2500	0.50	0.0159	8	0.034	Chasing
61	5	0.07	0.52	1.65	10.0	10.0	61115	61115	0.00	2500	0.50	0.0159	8	0.034	Chasing
62	2	0.04	0.54	1.86	6.0	8.0	36669	48892	0.14	2500	0.50	0.0159	8	0.034	Frag-Chasing
63	2	0.04	0.83	2.12	3.0	3.0	136604	136604	0.00	2500	0.26	0.0141	4	0.053	Frag-Chasing
64	1	0.02	0.71	1.96	2.7	3.0	122943	136604	0.05	2500	0.26	0.0141	4	0.053	Frag-Chasing
65	-1	-0.03	0.89	4.71	0.1	20.0	9549	1909860	0.99	2500	0.20	0.0141	3	0.068	Merging
66	2	0.03	1.56	2.66	10.0	10.0	61115	61115	0.00	2500	0.50	0.0159	8	0.034	Chasing
67	3	-0.08	3.59	6.63	0.1	20.0	9549	1909860	0.99	2500	0.20	0.0141	3	0.068	Merging
68	1	-0.02	3.39	5.89	0.3	14.0	28648	1336902	0.96	2500	0.20	0.0159	3	0.086	Exchange
69	3	-0.08	1.91	3.15	2.0	8.0	190986	763944	0.60	2500	0.20	0.0159	3	0.086	Frag-Chasing
70	3	0.07	1.95	3.41	1.0	8.0	95493	763944	0.78	2500	0.20	0.0141	3	0.068	Frag-Exchange

Figure S23. List of the tested conditions in the aligned configuration. η is the offset distance between the centroids, σ is the offset parameter, $\Delta x_b/D$ and $\Delta x_c/D$ are the initial distances between dune borders and centroids, respectively, normalized by the initial diameter of the impact pile, m_i and m_t are the masses of the impacting (upstream) and target (downstream) dunes, respectively, N_i and N_t are the number of grains of the impacting and target dunes, respectively, ξ_N is the dimensionless particle number, ρ_s and d are the density and mean diameter of grains, respectively, u_* is the shear velocity, Re_* is the particle Reynolds number, θ is the Shields number, and *Pattern* corresponds to the collision pattern.

Off-centered position															
#	η	σ	$\Delta x_b/D$	$\Delta x_c/D$	m_i	m_t	N_i	N_t	ξ_N	ρ_s	d	u_*	Re_*	θ	Pattern
-	(mm)	-	-	-	(g)	(g)	-	-	-	(kg/m ³)	(mm)	(m/s)	-	-	-
1	22	0.49	0.48	2.16	2.0	8.0	12223	48892	0.60	2500	0.50	0.0141	7	0.027	Merging
2	28	0.66	0.57	2.18	2.0	8.0	12223	48892	0.60	2500	0.50	0.0150	8	0.031	Merging
3	25	0.58	0.38	2.03	2.0	8.0	12223	48892	0.60	2500	0.50	0.0159	8	0.034	Merging
4	26	0.59	0.46	2.01	2.0	8.0	190986	763944	0.60	2500	0.20	0.0141	3	0.068	Frag-Exchange
5	17	0.39	0.43	2.15	2.0	8.0	190986	763944	0.60	2500	0.20	0.0159	3	0.086	Frag-Exchange
6	16	0.43	0.40	1.70	2.0	8.0	7453	29812	0.60	4100	0.50	0.0168	8	0.019	Merging
7	17	0.48	0.39	1.86	2.0	8.0	7453	29812	0.60	4100	0.50	0.0202	10	0.027	Merging
8	25	0.52	0.42	1.72	4.0	8.0	24446	48892	0.33	2500	0.50	0.0141	7	0.027	Chasing
9	22	0.47	0.60	1.94	4.0	8.0	24446	48892	0.33	2500	0.50	0.0159	8	0.034	Chasing
10	24	0.50	0.66	2.03	4.0	8.0	381972	763944	0.33	2500	0.20	0.0141	3	0.068	Chasing
11	27	0.60	0.30	1.77	4.0	8.0	381972	763944	0.33	2500	0.20	0.0159	3	0.086	Frag-Chasing
12	16	0.40	0.57	1.80	4.0	8.0	14906	29812	0.33	4100	0.50	0.0168	8	0.019	Chasing
13	15	0.38	0.40	1.68	4.0	8.0	14906	29812	0.33	4100	0.50	0.0202	10	0.027	Merging
14	24	0.57	0.79	2.69	1.0	8.0	6112	48892	0.78	2500	0.50	0.0141	7	0.027	Merging
15	22	0.51	0.73	2.68	1.0	8.0	6112	48892	0.78	2500	0.50	0.0159	8	0.034	Merging
16	21	0.52	0.41	2.37	1.0	8.0	95493	763944	0.78	2500	0.20	0.0141	3	0.068	Exchange
17	21	0.53	0.52	2.49	1.0	8.0	95493	763944	0.78	2500	0.20	0.0159	3	0.086	Exchange
18	18	0.40	1.09	2.67	1.0	8.0	45535	364277	0.78	2500	0.26	0.0159	4	0.067	Exchange
19	14	0.43	0.47	2.19	1.0	8.0	3727	29812	0.78	4100	0.50	0.0168	8	0.019	Merging
20	16	0.48	0.53	2.30	1.0	8.0	3727	29812	0.78	4100	0.50	0.0202	10	0.027	Merging
21	26	0.57	0.61	2.08	3.0	8.0	18336	48892	0.45	2500	0.50	0.0141	7	0.027	Chasing
22	23	0.49	0.63	2.02	3.0	8.0	18336	48892	0.45	2500	0.50	0.0159	8	0.034	Merging
23	19	0.40	0.82	2.28	3.0	8.0	136604	364277	0.45	2500	0.26	0.0141	4	0.053	Frag-Exchange
24	19	0.41	0.63	2.02	3.0	8.0	286479	763944	0.45	2500	0.20	0.0159	3	0.086	Frag-Chasing
25	19	0.43	0.78	2.26	3.0	8.0	286479	763944	0.45	2500	0.20	0.0176	4	0.106	Frag-Chasing
26	15	0.38	0.45	1.69	3.0	8.0	11181	29812	0.45	4100	0.50	0.0168	8	0.019	Merging
27	16	0.41	0.33	1.52	3.0	8.0	11181	29812	0.45	4100	0.50	0.0202	10	0.027	Merging
28	22	0.43	0.58	1.81	6.0	8.0	36669	48892	0.14	2500	0.50	0.0141	7	0.027	Chasing
29	17	0.32	0.62	1.89	6.0	8.0	36669	48892	0.14	2500	0.50	0.0159	8	0.034	Chasing
30	20	0.39	0.81	2.06	6.0	8.0	572958	763944	0.14	2500	0.20	0.0141	3	0.068	Chasing
31	21	0.41	0.53	1.94	6.0	8.0	572958	763944	0.14	2500	0.20	0.0159	3	0.086	Frag-Chasing
32	16	0.37	0.40	1.57	6.0	8.0	22359	29812	0.14	4100	0.50	0.0168	8	0.019	Chasing
33	15	0.37	0.39	1.61	6.0	8.0	22359	29812	0.14	4100	0.50	0.0202	10	0.027	Chasing
34	32	0.72	0.91	3.70	0.3	14.0	1833	85562	0.96	2500	0.50	0.0141	7	0.027	Merging
35	20	0.46	1.45	4.27	0.3	14.0	1833	85562	0.96	2500	0.50	0.0159	8	0.034	Merging
36	22	0.48	1.01	3.22	0.3	14.0	28648	1336902	0.96	2500	0.20	0.0141	3	0.068	Exchange
37	24	0.54	0.65	3.01	0.3	14.0	28648	1336902	0.96	2500	0.20	0.0159	3	0.086	Exchange
38	20	0.43	1.13	5.87	0.1	20.0	9549	1909859	0.99	2500	0.20	0.0141	3	0.068	Merging
39	17	0.38	1.27	5.45	0.1	20.0	9549	1909859	0.99	2500	0.20	0.0159	3	0.086	Exchange
40	15	0.42	0.89	3.28	0.5	6.0	47746	572958	0.85	2500	0.20	0.0141	3	0.068	Exchange
41	12	0.35	0.79	2.95	0.5	6.0	47746	572958	0.85	2500	0.20	0.0159	3	0.086	Exchange
42	19	0.49	0.90	2.16	3.0	3.0	286479	286479	0.00	2500	0.20	0.0141	3	0.068	Chasing
43	15	0.41	0.52	1.84	3.0	3.0	286479	286479	0.00	2500	0.20	0.0159	3	0.086	Chasing
44	14	0.34	0.68	1.80	3.0	3.0	136604	136604	0.00	2500	0.26	0.0141	4	0.053	Frag-Chasing
45	20	0.34	0.52	1.76	10.0	10.0	61115	61115	0.00	2500	0.50	0.0141	7	0.027	Chasing
46	20	0.33	0.59	1.83	10.0	10.0	61115	61115	0.00	2500	0.50	0.0159	8	0.034	Chasing
47	17	0.38	0.35	1.51	8.0	8.0	29812	29812	0.00	4100	0.50	0.0168	8	0.019	Chasing
48	16	0.37	0.43	1.60	8.0	8.0	29812	29812	0.00	4100	0.50	0.0202	10	0.027	Chasing
49	16	0.49	1.42	2.33	3.0	3.0	286479	286479	0.00	2500	0.20	0.0159	3	0.086	Chasing
50	16	0.41	2.78	6.22	0.1	20.0	9549	1909859	0.99	2500	0.20	0.0141	3	0.068	Merging
51	14	0.42	2.03	3.58	0.5	6.0	47746	572958	0.85	2500	0.20	0.0159	3	0.086	Exchange
52	27	0.63	1.22	2.29	6.0	8.0	572958	763944	0.14	2500	0.20	0.0159	3	0.086	Frag-Chasing
53	13	0.35	1.40	2.70	2.0	8.0	190986	763944	0.60	2500	0.20	0.0159	3	0.086	Frag-Exchange

Figure S24. List of the tested conditions in the off-centered configuration. η is the offset distance between the centroids, σ is the offset parameter, $\Delta x_b/D$ and $\Delta x_c/D$ are the initial distances between dune borders and centroids, respectively, normalized by the initial diameter of the impact pile, m_i and m_t are the masses of the impacting (upstream) and target (downstream) dunes, respectively, N_i and N_t are the number of grains of the impacting and target dunes, respectively, ξ_N is the dimensionless particle number, ρ_s and d are the density and mean diameter of grains, respectively, u_* is the shear velocity, Re_* is the particle Reynolds number, θ is the Shields number, and *Pattern* corresponds to the collision pattern.

August 19, 2020, 7:05pm

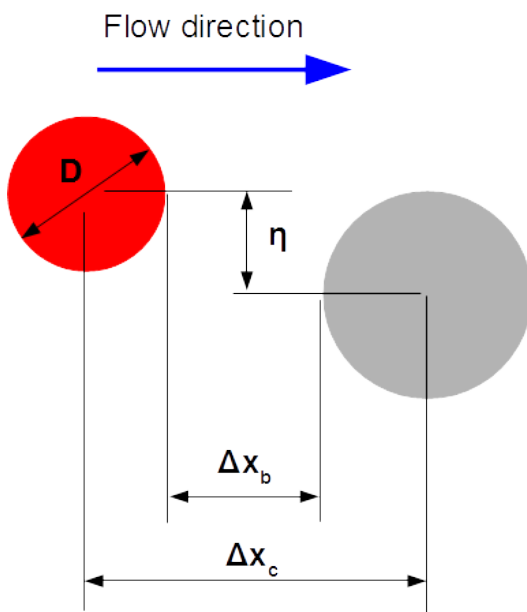


Figure S25. Offset distance, η , and initial distances between dune borders and centroids in the longitudinal direction, Δx_b and Δx_c , respectively, as listed in Figs. S23 and S24.

Table S1. Cross-sectional mean velocity U , shear velocity u_* , experimentally determined Darcy friction factor f , and Darcy friction factor from the Blasius correlation f_{bla} , for each Reynolds numbers Re and Re_{dh} .

Re	Re_{dh}	U	u_*	f	f_{bla}
...	...	m/s	m/s
2.43×10^4	1.65×10^4	0.243	0.0147	0.0293	0.0279
2.94×10^4	1.99×10^4	0.294	0.0173	0.0277	0.0266
3.64×10^4	2.47×10^4	0.364	0.0210	0.0266	0.0252

Table S2. Figure number, test number, area of the impact barchan A_i , area of the expelled barchan A_e , and ratio between areas of expelled and impact barchans A_e/A_i , for the exchange pattern. A_i and A_e correspond to averages over time of areas just before collision (for the impact barchan) and after being expelled (for the ejected barchan), respectively.

Figure #	Test #	A_i	A_e	A_e/A_i
...	...	mm ²	mm ²	...
S23	35	427	296	0.69
S23	36	337	559	1.66
S23	38	706	540	0.76
S23	39	1179	1852	1.57
S23	43	381	275	0.72
S23	44	401	638	1.59
S23	68	333	180	0.54
S24	17	401	638	1.59
S24	18	594	545	0.92
S24	36	378	659	1.74
S24	37	356	909	2.56
S24	39	136	81	0.59
S24	40	568	825	1.45
S24	41	466	981	2.10
S24	51	655	997	1.52